NASA Contractor Report 201691

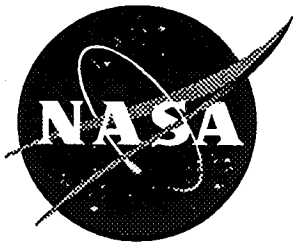

Effect of Pressure Gradients on Plate Response and Radiation in a Supersonic Turbulent Boundary Layer

Abdelkader Frendi
Analytical Services & Materials, Inc., Hampton, Virginia

Contracts NAS1-19700 and NAS1-96014

March 1997

National Aeronautics and
Space Administration
Langley Research Center
Hampton, Virginia 23681-0001

EFFECT OF PRESSURE GRADIENTS ON PLATE RESPONSE AND RADIATION IN A SUPERSONIC TURBULENT BOUNDARY LAYER

Abdelkader Frendi
Analytical Services and Materials, Inc.
Hampton, VA 23666

Abstract

Using the model developed by the author [1] for zero-pressure gradient turbulent boundary layers, results are obtained for adverse and favorable pressure gradients. It is shown that when a flexible plate is located in an adverse pressure gradient area, it vibrates more than if it were in a favorable pressure gradient one. Therefore, the noise generated by the plate in an adverse pressure gradient is much greater than that due to the plate in a favorable pressure gradient. The effects of Reynolds number and boundary layer thickness are also analysed and found to have the same effect in both adverse and favorable pressure gradient cases. Increasing the Reynolds number is found to increase the loading on the plate and therefore acoustic radiation. An increase in boundary layer thickness is found to decrease the level of the high frequencies and therefore the response and radiation at these frequencies. The results are in good qualitative agreement with experimental measurements.

1. Introduction

Pressure gradients in supersonic turbulent boundary layers arise in many practical engineering problems. For instance, the exterior curved surfaces of a high speed civilian and military aircraft, the engine inlets of such aircrafts, in turbomachinery and missiles. Because of the renewed interest in a civilian supersonic transport, scientists and engineers are investigating the problem of pressure gradients and their impact on structural fatigue and interior noise.

Spina *et al.* [2] wrote a review paper on the physics of supersonic turbulent boundary layers. In particular, an indepth discussion of adverse and favorable pressure gradients as well as streamline curvature was given. They stated that in an adverse pressure gradient boundary-layer, as the pressure increases, the boundary-layer thickness decreases and the wall-shear-stress increases. However, the exact opposite happens in a favorable pressure gradient boundary-layer. Concave streamline curvature (associated with adverse pressure gradients) tends to enhance mixing and therefore destabilize the boundary-layer; while convex curvature (associated with favorable pressure gradients) has a stabilizing effect.

A similar review article was written by Smith and Smits [3]. They highlighted the differences between subsonic and supersonic boundary-layers, in particular, the absence of similarity between the two cases in the presence of pressure gradients.

Bowersox and Buter [4] carried-out an experimental investigation of a Mach 2.9 turbulent boundary-layer with mild favorable and combined pressure gradients. They used Laser Doppler Velocimetry (LDV) and cross film anemometry to measure the Reynolds shear stress. They found that, in a favorable pressure gradient the shear stress was reduced by as much as 50 to 100%. Webster *et al.* [5] studied experimentally the turbulent statistics of a boundary layer over swept and unswept bumps. They observed that the boundary layer grew rapidly on the downstream side of the bump but did not separate. Also the meanflow profiles deviate significantly from typical logarithmic layer behavior.

In all the above studies, there was little or no-mention of the wall pressure fluctuations and how they are effected by pressure gradients. For interior noise and sonic fatigue, wall pressure fluctuations is an important quantity to measure. However, this is a very difficult measurement to make as the transducers have to be small enough in size and perfectly flush to the surface for such measurements to be meaningful. Maestrello [6] measured the wall pressure fluctuations in a wind tunnel at several supersonic Mach numbers in addition to the mean velocity profile and flexible panel response measurements. He found that strong coupling exists between the flow and the flexible panel response at these high speeds.

Computationally, in order to accurately calculate the wall pressure fluctuations, one needs to use Direct Numerical Simulation (DNS). However, this is not possible for realistic engineering problems. A Large Eddy Simulation (LES) calculation could be performed for simple engineering problems, however, models are still being formulated to accurately capture the subgrid scale contributions to the various physical phenomena. In the industrial world, empirical models are still the main tool used to represent wall pressure fluctuations. In particular, the Corcos [7] and Efimstov [8] models are widely used. However, these models do not take into account pressure gradients and surface curvature. In addition, they require experimental data in order to be used. Moreover, a recent LES calculation by Singer [9] showed that the Corcos model does a poor job at reproducing the correct coherence in directions that are at an angle with the downstream or cross-flow directions. Therefore, there is an urgent need for better models that represent the wall pressure fluctuations with or without pressure gradients and wall curvature.

In this paper, the mathematical model developed by the author [1] for zero pressure gradients is extended to account for favorable and adverse pressure gradients as well as wall curvature. A combination of concave and convex surfaces is chosen. In order to avoid the problem of shock-boundary-layer interaction, a smooth compression corner is used. The remainder of the paper is organized as follows; in section (2) the mathematical model is derived, the method of solution is described in section (3) and the results and discussion in section (4). The concluding remarks are given in section (5).

2. Mathematical Model

2.1 The Turbulent Boundary Layer Equations

Using the triple decomposition proposed by W.C. Reynolds [10], the flow quantities are decomposed as follows;

$$g = \tilde{g} + \hat{g} + g'' \tag{1}$$

where g represents a flow quantity and $(\tilde{g})$ its Favre averaged mean defined by

$$\tilde{g} = \frac{\overline{(\rho g)}}{\bar{\rho}}. \tag{2}$$

When decomposing the density, the turbulent fluctuations, ρ'', are neglected by virtue of Morkovin's hypothesis [11] which has been recently verified by Sommer *et al.* [12], therefore;

$$\rho = \bar{\rho} + \hat{\rho}. \tag{3}$$

In equations (1) and (3), $(\hat{g}, \hat{\rho})$ is the low frequency variation part of the mean and (g'') is the turbulent fluctuation.

By defining the total mean to be

$$G = \tilde{g} + \hat{g}, \tag{4}$$

equation (1) becomes

$$g = G + g''. \tag{5}$$

In the derivation of the dynamic equations used by W.C. Reynolds, a conditional averaging was introduced. Some properties of this averaging are;

$$\begin{gathered} < g'' >= 0 \qquad < \hat{g}f >= \hat{g} < f > \\ < \tilde{g}f >= \tilde{g} < f > \qquad \widetilde{< g >} = \tilde{g} =< \tilde{g} > \\ \widetilde{\hat{g}f''} = < \widetilde{\hat{g}f''} > = 0. \end{gathered} \tag{6}$$

Using the decomposition given by equation (5) in the continuity, momentum, energy and state equations along with the conditional averaging and Einstein summation convention one arrives at the following mass, momentum, energy and state equations;

$$\frac{\partial \rho}{\partial t} + \frac{\partial}{\partial x_i}(\rho U_i) = 0, \qquad i = 1, 2, 3 \tag{7}$$

$$\frac{\partial}{\partial t}(\rho U_i) + \frac{\partial}{\partial x_j}\left[\rho U_i U_j - < \tau_{ij} > + \rho < u_i'' u_j'' >\right] + \frac{\partial P}{\partial x_i} = 0, \qquad i, j = 1, 2, 3 \tag{8}$$

$$\frac{\partial E}{\partial t} + \frac{\partial}{\partial x_j}\left[(E + P)U_j - < \tau_{ij} > U_j + < e'' u_j'' > + < p'' u_j'' > - < \tau_{ij} u_j'' >\right] = 0 \tag{9}$$

$$P = (\gamma - 1)\left[E - \rho(U_1^2 + U_2^2 + U_3^2 + < (u_1'')^2 > + < (u_2'')^2 > + < (u_3'')^2 >)/2\right]. \quad (10)$$

In equations (7)-(10), (ρ, U_i, E, P) represent the total means of the variables (ρ, u_i, e, p), while (u_i'', u_j'', e'', p'') are the turbulent fluctuations. The variable (e) is the total energy defined as $e = p/(\gamma - 1) + \rho(u_1^2 + u_2^2 + u_3^2)/2$. In equations (8) and (9), $< \tau_{ij} >$ is the conditionally averaged stress tensor,

$$< \tau_{ij} >= \frac{M_\infty}{Re_L}\left[\mu\left(\frac{\partial U_i}{\partial x_j} + \frac{\partial U_j}{\partial x_i}\right) - \frac{2}{3}\mu\frac{\partial U_k}{\partial x_k}\delta_{ij}\right], \quad (11)$$

where M_∞, Re_L and μ are the freestream Mach number, Reynolds number and molecular viscosity, respectively. The term $< u_i'' u_j'' >$ of equation (8) is similar to the Reynolds stress tensor and is modeled in the same way. In equation (9), $< e'' u_j'' >$, $< p'' u_j'' >$ and $< \tau_{ij} u_j'' >$ have to be modeled.

Invoking the Boussinesq approximation that the Reynolds stress tensor is proportional to the mean strain-rate tensor, leads to

$$\rho < u_i'' u_j'' >= \frac{2}{3}\rho k \delta_{ij} - 2\mu_t(S_{ij} - \frac{1}{3}S_{kk}\delta_{ij}) \quad (12)$$

where $k =< u_i'' u_i'' > /2$ is the turbulent kinetic energy, μ_t is the turbulent eddy viscosity and S_{ij} is the mean strain-rate tensor given by,

$$S_{ij} = \frac{1}{2}\left[\frac{\partial U_i}{\partial x_j} + \frac{\partial U_j}{\partial x_i}\right]. \quad (13)$$

The turbulent eddy viscosity is obtained from the relation

$$\mu_t = C_\mu^\star \frac{\rho k}{\omega} \quad (14)$$

where $C_\mu^\star$ is a constant, ω the specific dissipation rate (ϵ/k) with ϵ being the dissipation.

The conservation equations for k and ω are;

$$\frac{\partial}{\partial t}(\rho k) + \frac{\partial}{\partial x_j}(\rho U_j k) = -\rho < u_i'' u_j'' > \frac{\partial U_i}{\partial x_j} - \rho\omega k + \frac{\partial}{\partial x_j}\left(\frac{\mu_{tl}}{\sigma_k}\frac{\partial k}{\partial x_j}\right) \quad (15)$$

$$\frac{\partial}{\partial t}(\rho\omega) + \frac{\partial}{\partial x_j}(\rho U_j \omega) = -\rho C_{\omega_1}\frac{\omega}{k} < u_i'' u_j'' > \frac{\partial U_i}{\partial x_j} - C_{\omega_2}\rho\omega^2 + \frac{\partial}{\partial x_j}\left(\frac{\mu_{tl}}{\sigma_\omega}\frac{\partial \omega}{\partial x_j}\right). \quad (16)$$

In equations (15) and (16), $\mu_{tl} = C_{\mu l}^\star \rho(k/\omega)$ and $C_{\omega_1} = C_{\omega_2} - \kappa^2/((C_{\mu l}^\star)^{0.5}\sigma_\omega)$, with $C_{\mu l}^\star = 0.09$ (same as $C_\mu^\star$ in the log layer), $\sigma_k = \sigma_\omega = 2$, $C_{\omega_2} = 0.83$ and $\kappa = 0.41$. The model described above was derived by Wilcox [13] and is known as the (k-ω) turbulence model.

2.2 The Plate Equation

The out-of-plane plate displacement, w, is given by the biharmonic equation,

$$D\Delta^2 w + \rho_p h \frac{\partial^2 w}{\partial t^2} + \Gamma \frac{\partial w}{\partial t} = \delta p \tag{17}$$

where D is the plate stiffness obtained from $D = E_p h^3/12(1-\nu_p^2)$, with E_p being the Young Modulus, h the plate thickness and ν_p the Poisson ratio. In equation (17), ρ_p is the plate material density and Γ is the structural damping. The biharmonic term is defined as

$$\Delta^2 = \frac{\partial^4}{\partial x^4} + 2\frac{\partial^4}{\partial x^2 \partial y^2} + \frac{\partial^4}{\partial y^4} \tag{18}$$

The right hand side, δp, of equation (17) represents the pressure loading due to the adjacent fluids and can be written as

$$\delta p = p^a - p^{bl} \tag{19}$$

with (p^a) being the radiated acoustic pressure and (p^{bl}) the turbulent boundary layer pressure calculated from the model in section (2.1).

2.3 The Acoustic Radiation Equation

In order to calculate the pressure p^a of equation (19), Kirchhoff's formula is used to arrive at (see ref. [14] for details)

$$p^a(x,y,z,t) = \frac{\rho_\infty}{2\pi} \int\int_D \frac{[w_{tt}(\tau, x', z')]}{R} dx' dz' \tag{20}$$

where the integration domain, D, is over the whole plate and $w_{tt} = \frac{\partial^2 w}{\partial t^2}$. In equation (20), the square brackets, [.], are used to denote a retarded time, i.e.

$$[w_{tt}(\tau, x', z')] = w_{tt}(t - R/c_\infty, x', z') \tag{21}$$

where $R = [(x-x')^2 + y^2 + (z-z')^2]^{1/2}$ is the distance from an observer point (x,y,z) to a point on the plate $(x',0,z')$. In equation (21), c_∞ is the speed of sound. Equation (20) is used to calculate the pressure both on the surface of the plate and in the far-field. When using equation (20) to calculate the surface pressure, a Taylor series expansion of the integrand is used to avoid the singularity at $R = 0$ (when the observer point coincides with the source).

3. Method of Solution

The turbulent boundary layer equations are solved using the three-dimensional thin-layer Navier-Stokes code known as CFL3D. [15] The numerical method uses a second order accurate finite volume scheme. The convective terms are discretized with an upwind

scheme that is based on Roe's flux difference splitting method, while all the viscous terms are centrally differenced. The equations are integrated in time with an implicit, spatially split approximate-factorization scheme. The thin-layer approximation retains only those viscous terms with derivatives normal to the body surface. This is generally considered to be a good approximation for high-Reynolds-number aerodynamic flows with minimal separation. Two calculations are made for each case; first the steady state mean velocity profiles are obtained using a large domain that includes the leading edge of the plate, then using a smaller domain downstream of the leading edge an unsteady calculation is carried out by perturbing the mean velocity profile at the inflow boundary as follows

$$u = \tilde{u} + \epsilon R_n(y, z, t). \tag{22}$$

In equation (22), $R_n(y, z, t)$ is a random number generated using an IMSL routine called RNNOF [16] and ϵ is a small amplitude chosen to be between 0.05 and 0.25. In the steady state calculation, the flow in the region upstream of the plate's leading edge is specified as laminar, while that downstream of the leading edge is turbulent. The plate equation (17) is integrated using an implicit finite difference method for structural dynamics developed by Hoff and Pahl. [17] The radiated acoustic pressure, p^a, is obtained through a combination of the Simpson and trapezoidal rules of integration in the (x, z) directions [14].

Coupling between the plate and the acoustic and boundary layer pressure fields is obtained as follows. Using the previous time step plate velocity and acceleration as boundary conditions, the turbulent boundary layer equations (7)-(10), (15), (16) and the acoustic equation (20) are integrated to obtain the new surface pressure fields, these are then used to update the plate equation. This procedure is repeated at every time step.

4. Results and Discussion

This section is divided into several subsections. In subsection (4.1) results from a large three dimensional computation with adverse and favorable pressure gradients are presented. Comparisons to experiments are given in section (4.2). The effects of boundary layer thickness are analysed in subsection (4.3) and that of Reynolds number in subsection (4.4).

4.1 Combined Adverse and Favorable Pressure Gradients

The flow and structural properties used in this case are as follows; free-stream Mach number $M_\infty = 2.4$, free-stream temperature $T_\infty = 560\ R$, wall temperature $T_w = 550\ R$ and Reynolds number per foot $Re/ft = 3.\text{x}10^6$. Two titanium plates having the following parameters are used; length $a = 12$ inches, width $b = 6$ inches, thickness $h = 0.062$ inches, density per unit area $\rho_p h = 2.315\text{x}10^{-5}$ lbf·sec^2/in^3, stiffness $D = 345.$ lbf·in and damping $\Gamma = 7.4\text{x}10^{-4}$ lbf·sec/in^3. The excitation amplitude is set to $\epsilon = 0.08$.

The computational domain shown on fig. 1 is 4x1x1.5 ft in the streamwise, spanwise and vertical directions, respectively. The number of points used in the respective directions are, 197x49x81. The bottom surface of the computational domain contains a smooth bump together with horizontal surfaces. The dimensions of the smooth bump are 3x1x0.2 ft in the respective directions. The two flexible plates are located downstream of the concave

and convex parts of the bump. The plate centers are located at $x = 1.3$ ft and $x = 2.7$ ft in the downstream direction, respectively. The grid is uniform in the streamwise and spanwise directions and is stretched in the vertical direction as shown by the figure. The figure shows a higher density of vertical grid points near the wall. The radiated noise is computed at two positions having the following coordinates, (2., 0.5, 0.) ft and (2., 0.5, -4.8) ft. The fluid in the acoustic radiation region has the same properties as that in the supersonic flow region.

Figure 2 shows a three dimensional contour plot of the nondimensional static pressure. Most of the pressure changes occur over the smooth bump. Over the concave region of the bump, the pressure increases smoothly from 0.71 to 1.4 and then decreases back to 0.71 at the top of the bump. Over the convex region of the bump, the pressure decreases from 0.71 to 0.3 then increases back to 0.71. Figure 3 shows the three dimensional static pressure surfaces in regions of large gradients. Near the leading edge of the bump, the pressure increases rapidly, resulting in a series of compression waves that coalesce into an oblique shock-wave away from the surface. Near the top of the bump, the pressure decreases rapidly generating a series of expansion waves away from the surface. Another oblique shock wave is generated by the trailing edge of the bump. The three-dimensional Mach number contours, fig. 4, show the flow decelerating from $M_\infty = 2.4$ to $M_\infty = 2.$ in the concave region of the bump and then accelerating back to $M_\infty = 2.5$ in the convex region. The oblique shock wave and expansion fans are clearly shown by the figure. The concave region of the bump where the pressure increases and the Mach number decreases will also be referred to as the *adverse pressure gradient* region, while the convex part of the bump where the pressure decreases and the Mach number increases will be referred to as the *favorable pressure gradient* region. Figure 5 shows the mean velocity profile at various downstream locations. At $x = 0.5$ ft, just before the bump, $u/u_e = 1.$ everywhere except near the wall. For $0.5 < x < 2.$, adverse pressure gradient region, $u < u_e$ corresponding to a decelerated flow. For $2. < x < 3.5$, favorable pressure gradient region, $u > u_e$ corresponding to an accelerated flow.

The unsteady calculation was run using an excitation amplitude of $\epsilon = 0.08$ together with a broadband random noise in space and time (eqn. (22)). Figure 6 shows the power spectral density (PSD) of the pressure at the center of the two flexible plates. The level of the PSD of the pressure in the favorable pressure gradient region is everywhere lower than that in the adverse pressure gradient region. This is due to a decrease in the pressure fluctuations over that region. However, the decrease is more pronounced at higher frequencies (4000 to 6000 Hz) than it is at lower frequencies (0 to 2000 Hz) due to the combined effect of thicker boundary layer and reduced pressure fluctuations. Above 6000 Hz, there is little difference between the two PSDs as both the physical and numerical dissipation become dominant at high frequencies. Boundary layer thickness effect will be discussed in section [4.3]. A strong low frequency component, near zero, is observed in the favorable pressure gradient PSD. The PSDs of the displacement response at the center of the two plates are shown on fig. 7. As expected, the response of the plate located in the adverse pressure gradient region is higher than that of the plate located in the favorable pressure gradient region. The response obtained above 2000 Hz is not meaningful because of the lack of numerical resolution on the panels. For both plates, the response is dominated

by the first mode. The time histories of the radiated pressure from each plate and the total radiated pressure are shown on figs. 8a-c. The point at which the radiated pressure is calculated is located 0.5 ft away from the center of the two plates. Figures 8a and 8c, corresponding to acoustic radiation from the adverse pressure gradient plate and the total radiation from both plates, respectively; are nearly identical. The acoustic radiation from the plate located in the favorable pressure gradient is shown on fig. 8b. From this result one concludes that the total acoustic radiation, fig. 8c, is dominated by that of the plate located in the adverse pressure gradient region. The PSDs of the radiated acoustic pressure from the two plates are shown on fig. 9. The figure shows that the panel located in the adverse pressure gradient region radiates more than the one located in the favorable pressure gradient region at all frequencies. The difference is more pronounced at higher frequencies than it is at lower frequencies. In particular, the difference is small at the first mode which appears as a strong peak in the PSD of the favorable pressure panel radiation. Both PSDs show the presence of distinct peaks in the decaying part of the spectrum.

Figure 10 shows the instantaneous vertical fluid velocity distribution over the bottom rigid and flexible surfaces. A non-zero vertical velocity is shown in the regions where the flexible plates are located. This figure shows the coupling effects on the fluid vertical velocity. Figure 11 shows the instantaneous displacement response for both flexible plates. Since the excitation is symmetric in the spanwise direction, both plates show symmetric displacement responses. The plate located in the adverse pressure gradient region shows a (3,1) mode type displacement response, while the plate located in the favorable pressure gradient region shows a (1,1) mode type response. At another instant in time, this displacement response behavior might show a different combination of symmetric modes.

4.2 Comparisons to Experiments

As mentioned in the introduction, several experiments have been conducted to access the effects of pressure gradients in both subsonic and supersonic flow regimes. Several flow quantities were measured, however, no measurement was reported on the wall pressure fluctuations. In this sub-section, comparisons of the numerical results obtained using the geometry and flow conditions given in sub-section 4.1 to the measurements of Bowersox and Buter [4] and Webster *et al.* [5], are made. Figure 12a shows the nondimensional static pressure measured by Bowersox along the streamwise direction, for the favorable and combined (adverse and favorable) pressure gradients. The figure shows that the pressure decreases with downstream distance for the favorable pressure gradient case (dashed curve), while it increases for some distance x and then decreases in the combined case. Figure 12b shows the nondimensional Favre averaged Reynolds stress ($\tau_{xy}/\overline{\rho u}^2$) as a function of the nondimensional vertical distance(y/δ) measured in the favorable, zero and combined pressure gradients regions. The Favre averaged Reynolds stresses are the smallest in the favorable pressure gradient region and are nearly identical in the zero and combined pressure gradient regions. Moreover, in the favorable pressure gradient region, the Favre averaged Reynolds stresses are nearly zero for $y/\delta > 0.4$, while for the other two cases, the Favre averaged Reynolds stresses become zero only outside the boundary layer.

Figure 13a shows the streamwise nondimensional pressure distribution obtained numerically for the geometry and flow conditions given in sub-section 4.1. As shown by the

figure, adverse, favorable and zero pressure gradients regions exist. The pressure increases until it reaches a maximum at the middle of the concave surface then starts decreasing to a minimum value at the middle of the convex surface, then increases back to its starting value. The pressure before and after the bump remains constant (zero pressure gradient regions). Figure 13b shows a nondimensional Favre averaged Reynolds stress as a function of the nondimensional vertical distance at three locations in the zero, adverse and favorable pressure gradient areas, respectively. The zero pressure gradient area considered is the one before the bump. The adverse pressure gradient location is near the center of the concave surface, while the favorable pressure gradient location is near the middle of the convex surface. The figure shows that in the favorable pressure gradient area, the Favre averaged Reynolds stresses are much smaller than those in adverse and zero pressure gradient areas which is in agreement with the measurement of Bowersox and Buter [4]. However, the numerical results show that the Favre averaged Reynolds stresses are very small over a larger portion of the boundary layer for the favorable pressure gradient case. This difference may be due to the turbulence model used. In agreement with Bowersox and Buter's results [4], the zero and adverse pressure gradient Favre averaged Reynolds stress are nearly identical. The nondimensionalization used by Bowersox and Buter [4] is different from the one used in this paper, which explains the difference in the Favre averaged Reynolds stress scales.

Figure 14 shows the nondimensional mean velocity profile obtained by this calculation in the various regions of the domain. In the zero pressure gradient area ahead of the bump, the mean velocity profile shows a smooth variation. In the adverse pressure gradient region near the center of the concave surface, the velocity profile shows a reduction in speed in the outer region of the boundary layer, compared to the zero pressure gradient case, followed by a sharp rise due to the presence of an oblique shock wave. In the favorable pressure gradient case, the velocity is higher than that of the favorable pressure gradient case for $10^{-3} < y/\delta < 10^{-1}$ then becomes lower for $10^{-1} < y/\delta < 10$ before going through a jump back to $u/U_e = 1$. The behavior of the velocity profile in the favorable pressure gradient region is affected by the adverse pressure gradient area and the presence of the oblique shock wave. Qualitatively, this behavior is similar to that observed by Bowersox and Buter [4]. Figure 15 shows the skin friction coefficient as a function of the downstream distance. Near the leading edge of the bump, the skin friction goes through a sharp jump before undergoing a smoother variation over the concave and convex areas of the bump. The behavior of the skin friction over the bump is similar to that of the pressure (fig.13a).

4.3 Effects of Boundary-Layer Thickness

The effects of boundary-layer thickness on the plate response and radiation are analysed for both adverse and favorable pressure gradients. The approach used in both cases is the same; i.e. the flexible plate is placed 1 ft and 3 ft away from the leading edge, respectively. The computational domains used in the favorable and adverse pressure gradient calculations are shown on figs. 16a-b. In the favorable pressure gradient case, a diverging channel is used to accelerate the flow, fig. 16a. In the adverse pressure gradient case, the bottom surface is smoothly curved upward to decelerate the flow, fig. 16b. The same number of grid points is used in both cases; i.e. 197x81x49 in the streamwise, vertical and spanwise directions, respectively. Typical velocity profiles at the two locations are shown

on fig. 17 for a favorable pressure gradient case. The velocity profile at 3 ft shows a thicker boundary layer than that at 1 ft. The velocity profiles for the adverse pressure gradient case are similar. Figures 18a-b show the PSDs of the wall pressure fluctuation and the plate's vertical velocity both taken at the plate's center for the favorable pressure gradient case. The PSD of the wall pressure fluctuation shows that at both locations the level of the low frequencies is the same while that of the high frequencies is different, fig. 18a. At 3 ft, the high frequencies have a lower level than that at 1 ft. The figure shows also that the peak frequency has shifted to the lower frequencies at the 3 ft location. This is partly explained by the fact that as the boundary layer grows thicker, the large scale structures become more dominant. Another possible mechanism that could explain this difference is the combination of viscous and numerical damping. In order to check the effects of the later mechanism a finer grid was used, the results were found to be nearly identical with a negligible difference at high frequencies. The PSD of the center plate vertical velocity shows the presence of several peaks corresponding to the symmetric modes of the plate, fig. 18b. When the center is located at 3 ft away from the leading edge, the high frequency peaks have a lower amplitude than when it is located at 1 ft. This is in agreement with the PSD of the wall pressure fluctuation. Figures 19a-b show similar results for the adverse pressure gradient case. The wall pressure fluctuation PSD, fig. 19a, shows that the high frequencies have a lower level at 3 ft than at 1 ft. Note that the shifting of the peak is not as pronounced in this case. Similarly, the PSDs of the center plate vertical velocity, fig. 19b, show little or no-difference at low frequencies and a significant difference at high frequencies.

4.4 Effects of Reynolds Number

Two different Reynolds numbers are used in this study for both the adverse and favorable pressure gradients. The Reynolds numbers chosen are $3x10^6$ and $12x10^6$. Figures 20a-b show the PSDs of the fluctuating surface pressure and vertical velocity at the plate center for the favorable pressure gradient case. The PSDs of the surface pressure fluctuation, fig. 20a, show that the curve corresponding to the Reynolds number $12x10^6$ has a higher level than that for the Reynolds number $3x10^6$ over the entire frequency range. This is due to the fact that at higher Reynolds numbers, the wall shear-stress increases leading to an increase in wall pressure. As a results, the increased loading on the plate leads to an increase in the response at higher Reynolds numbers, as shown on fig. 20b. A similar result is obtained in the adverse pressure gradient case as shown on figs. 21a-b. One should note that the levels of all PSDs is higher in the adverse pressure gradient case, figs. 21a-b, than it is in the favorable one, figs. 20a-b.

5. Concluding Remarks

The results presented in this paper show that;

- Results are in good qualitative agreement with experiments.
- Adverse pressure gradients lead to an increase in plate loading and therefore its response and radiation are increased.
- Favorable pressure gradients lead to a decrease in plate loading and therefore its response and radiation are reduced.

- An increase in Reynolds number leads to an increase in plate loading and therefore response and radiation.
- As the boundary layer thickness increases, the high frequency content is reduced and their energy content transferred to the low frequencies.

Acknowledgements

The author would like to acknowledge the support of the Structural Acoustics Branch of NASA Langley Research Center under contracts NAS1-19700 and NAS1-96014. Dr. Stephen Rizzi was the technical monitor.

References

[1] Frendi, A., "On the coupling between a supersonic turbulent boundary layer and a flexible structure", *AIAA* Journal, Vol. 35, No. 1, pp. 58-66, January 1997.

[2] Spina, E.F., Smits, A.J. and Robinson, S.K., "The physics of supersonic turbulent boundary layers", *Ann. Rev. Fluid Mech.*, Vol. 26, 1994, pp. 287-319.

[3] Smith, D.R. and Smits, A.J., "The effects of Streamline Curvature and Pressure Gradients on the Behavior of Turbulent Boundary Layers in Supersonic Flow", AIAA 94-2227, 1994.

[4] Bowersox R.D.W. and Buter T.A., "Mass-Weighted Turbulence Measurements in a Mach 2.9 Boundary Layer Including Mild Pressure Gradients", AIAA 96-0659, 1996.

[5] Webster, R.D., DeGraaff, D.B. and Eaton, J.K., "Turbulent Statistics of a Boundary Layer over Swept and Unswept Bumps", AIAA 96-0658, 1996.

[6] Maestrello, L., "Radiation from and Panel Response to a Supersonic Turbulent Boundary Layer", *Journal of Sound and Vib.*, Vol. 10, No. 2, 1969, pp. 261-295.

[7] Corcos, G.M., "Resolution of pressure in turbulence," *The journal of the Acoustical Society of America*, vol. 35, no. 2, 1963, pp. 192-198.

[8] Efimtsov, B.M., "Characteristics of the field of turbulent wall pressure fluctuations at large Reynolds numbers," *Soviet Physical Acoustics*, vol. 28, no. 4, 1982, pp. 289-292.

[9] Singer, B.A., "Turbulent wall-pressure fluctuations: New model for off-axis cross-spectral density", NASA Contractor Report 198297, March 1996.

[10] Reynolds, W.C., and Hussain, A.K.M.F., "The mechanics of an organized wave in turbulent shear flow. Part 3: Theoretical models and comparisons with experiments," *Journal of Fluid Mechanics*, vol. 54, part 2, 1972, pp. 263-288.

[11] Morkovin, M., "Effects of compressibility on turbulent flows," Mecanique de la turbulence, CNRS, edited by A. Favre, published by Gordon and Breach, 1962, pp. 367-380.

[12] Sommer, T.P., So, R.M.C., and Gatski, T.B., "Verification of Morkovin's hypothesis for the compressible turbulence field using direct numerical simulation data," AIAA paper 95-0859, 33rd Aerospace Sciences Meeting and Exhibit, Reno, NV, 1995.

[13] Wilcox, D.C., "Reassessment of the scale-determining equation for advanced turbulence models," *AIAA Journal*, vol. 26, no. 11, 1988, pp. 1299-1310.

[14] Frendi, A., Maestrello, L., and Ting, L., "An efficient model for coupling structural vibrations with acoustic radiation," *Journal of Sound and Vibration*, vol. 182, no. 5, 1995, pp. 741-757.

[15] Rumsey, C., Thomas, J., Warren, G., and Liu, G., "Upwind Navier-Stokes solutions for separated periodic flows," AIAA paper 86-0247, 1986.

[16] International Mathematical and Statistical Library (IMSL), version 2.0, vol. 3, Houston, TX, 1991, pf. 1317.

[17] Hoff, C., and Pahl, P.J., "Development of an implicit method with numerical dissipation from generalized single-step algorithm for structural dynamics," *Comp. Meth. Appl. Mech. Eng.*, vol. 67, no. 2, 1988, pp. 367-385.

Figure 1: 3D Computational domain.

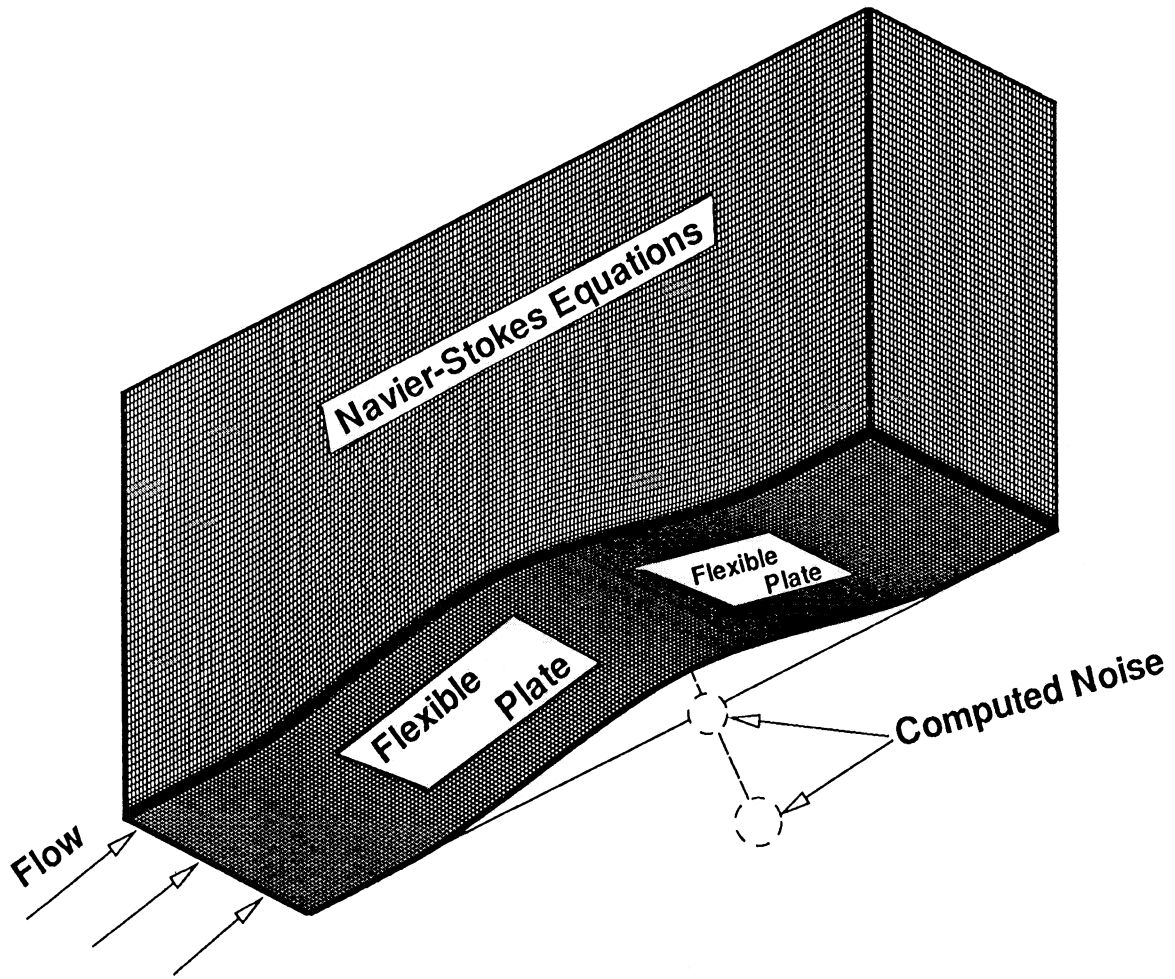

Figure 2: 3D Static pressure contours.

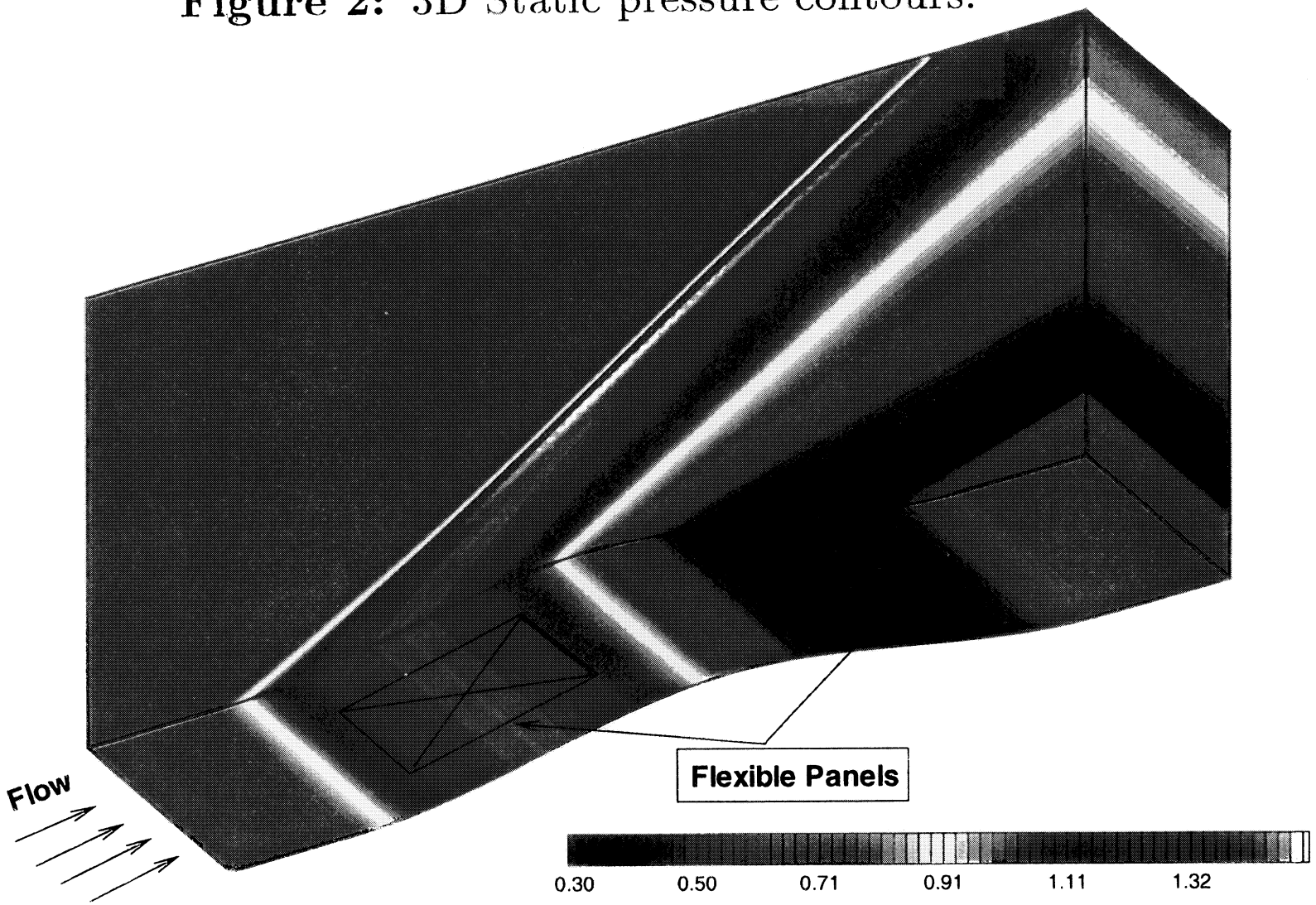

Figure 3: 3D Static pressure surfaces.

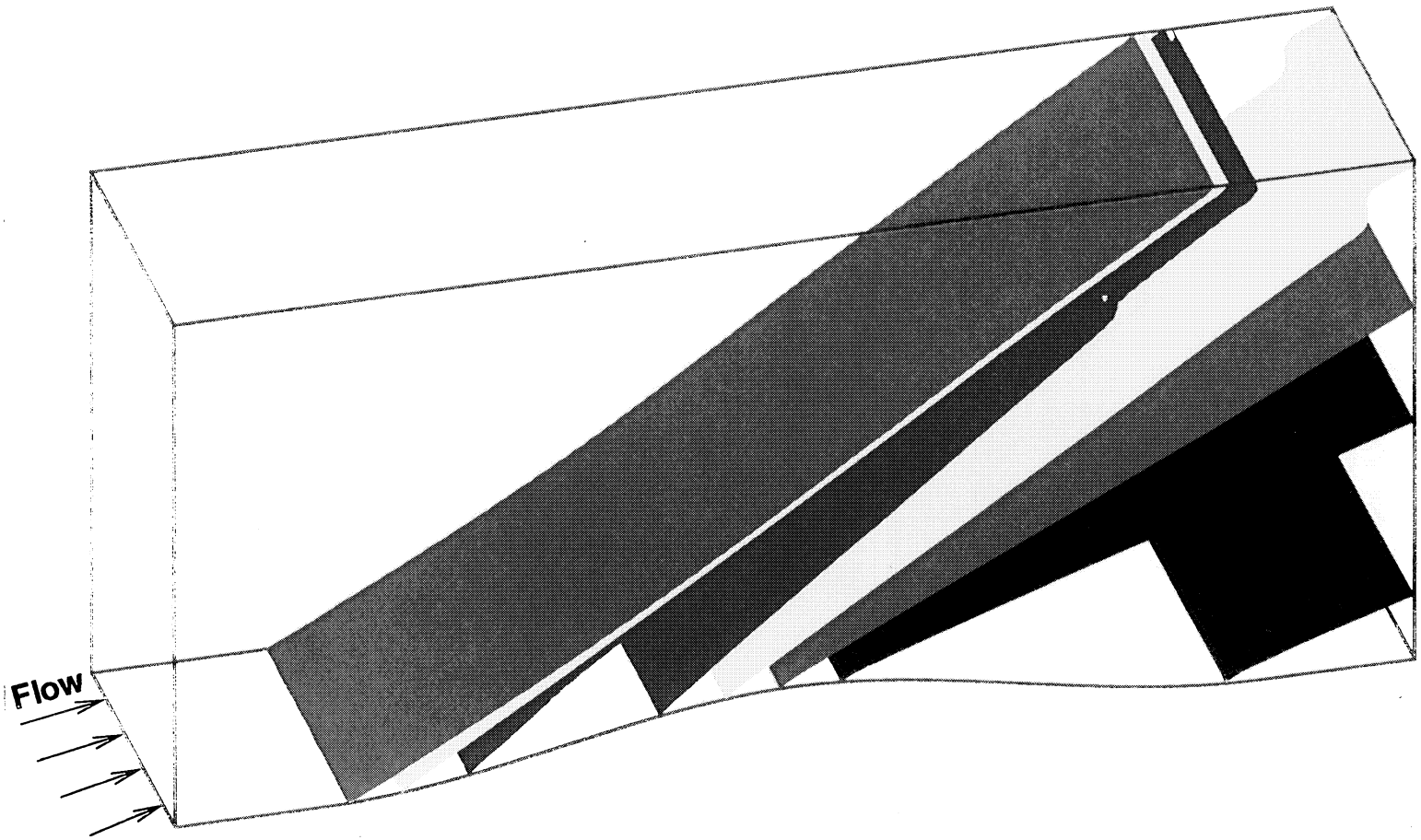

Figure 4: 3D Mach number contours.

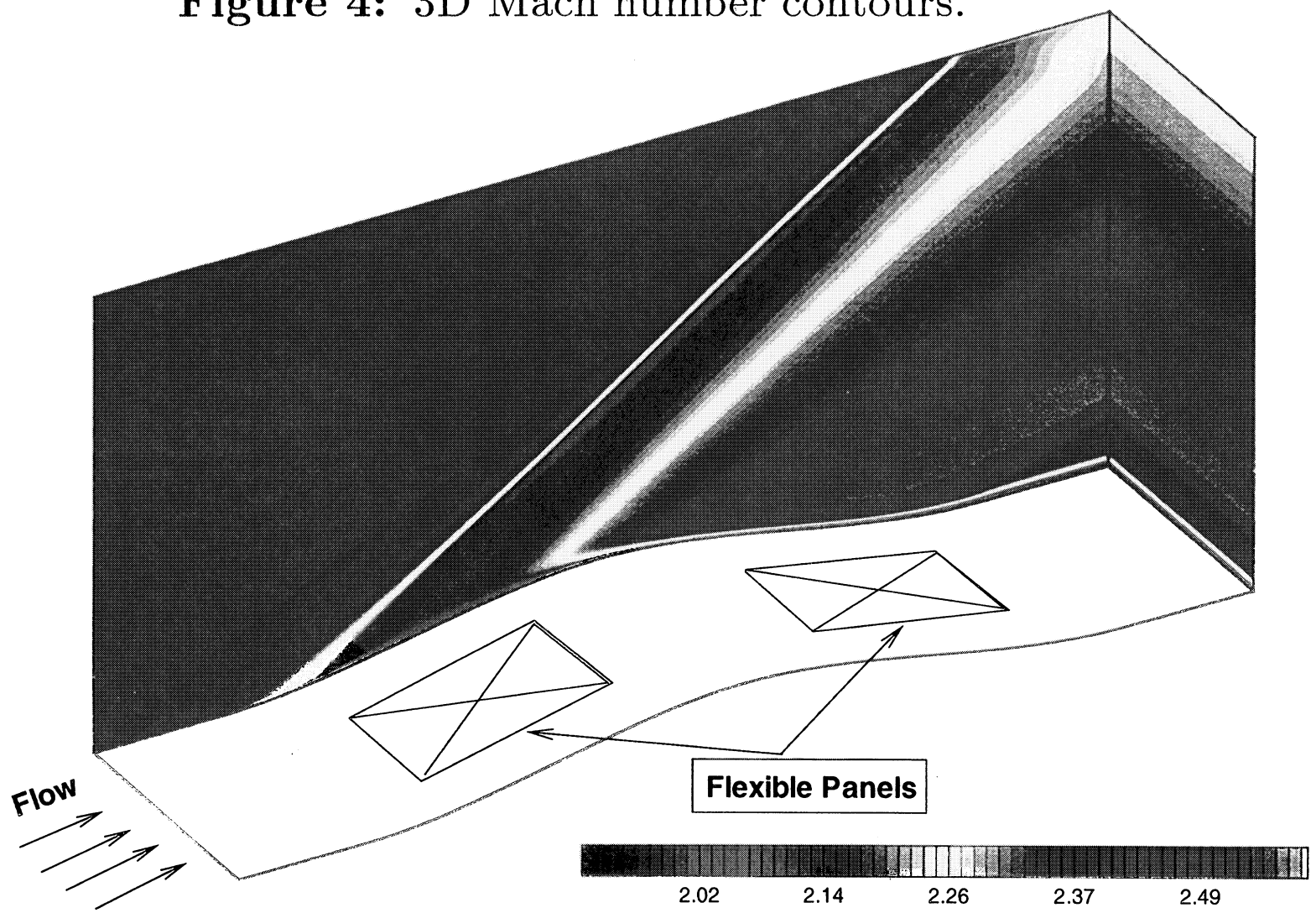

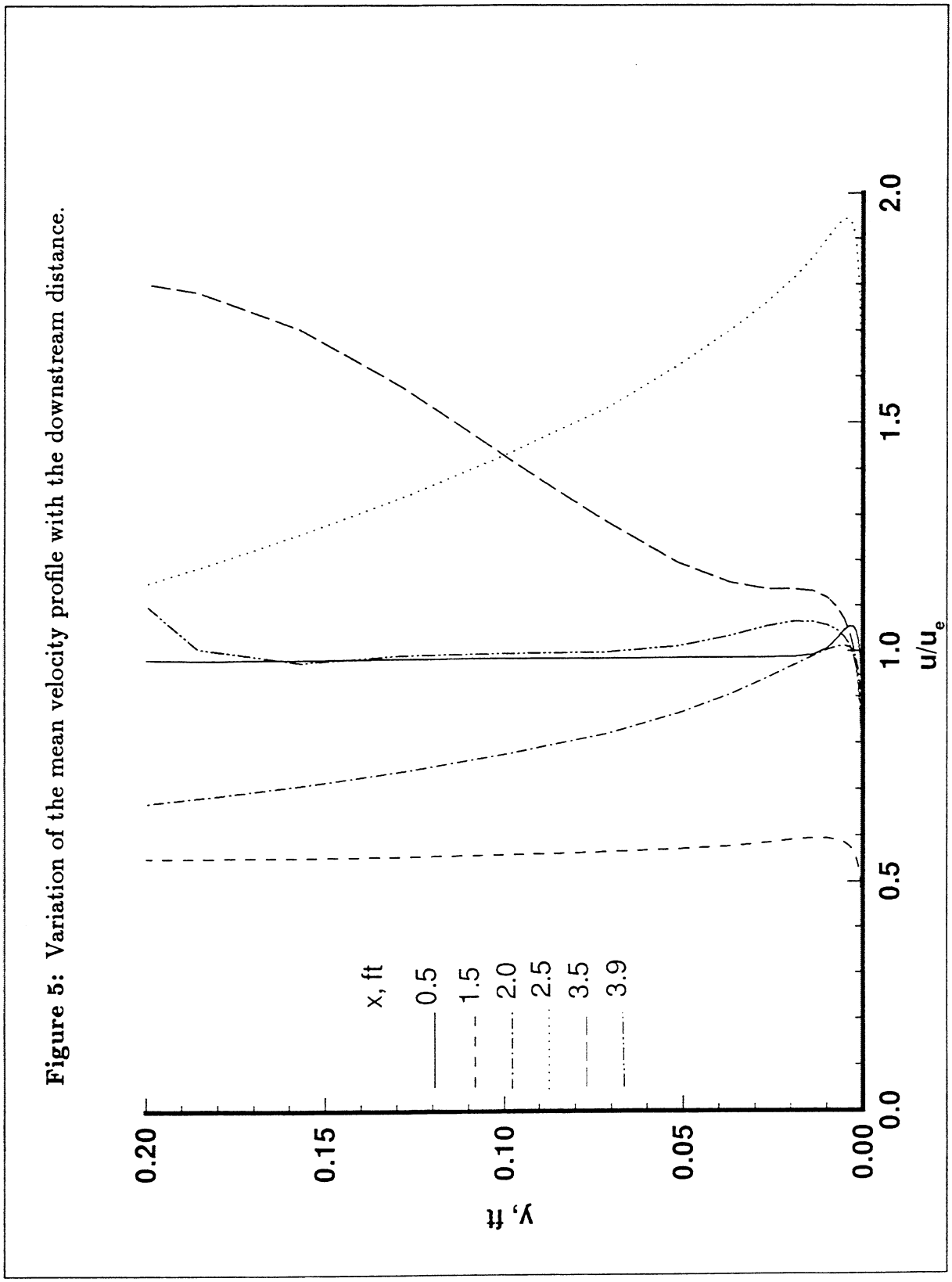

Figure 5: Variation of the mean velocity profile with the downstream distance.

Figure 6: PSD of the pressure fluctuation at the center of the two flexible plates.

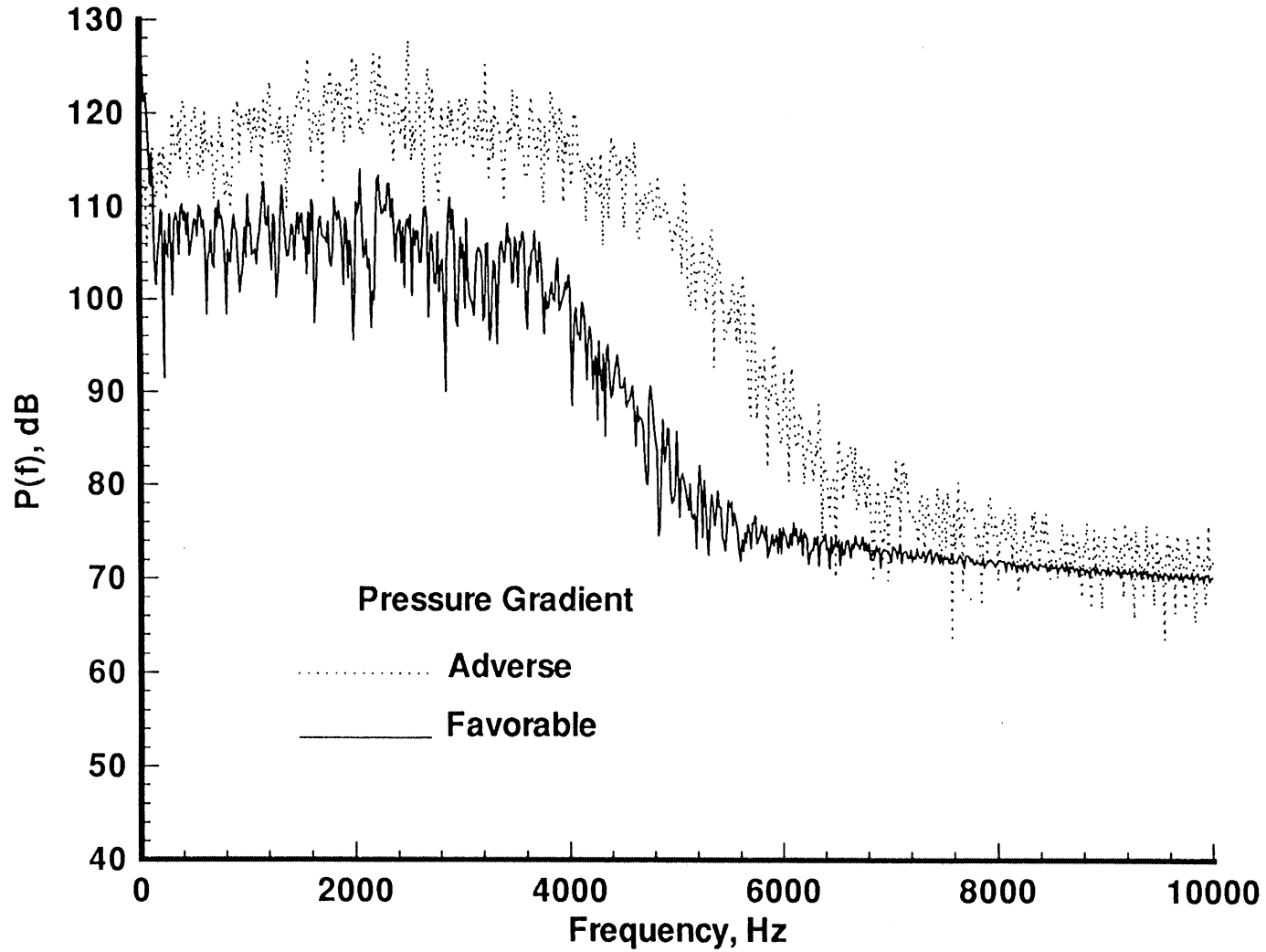

Figure 7: PSD of the displacement response at the center of the two flexible plates.

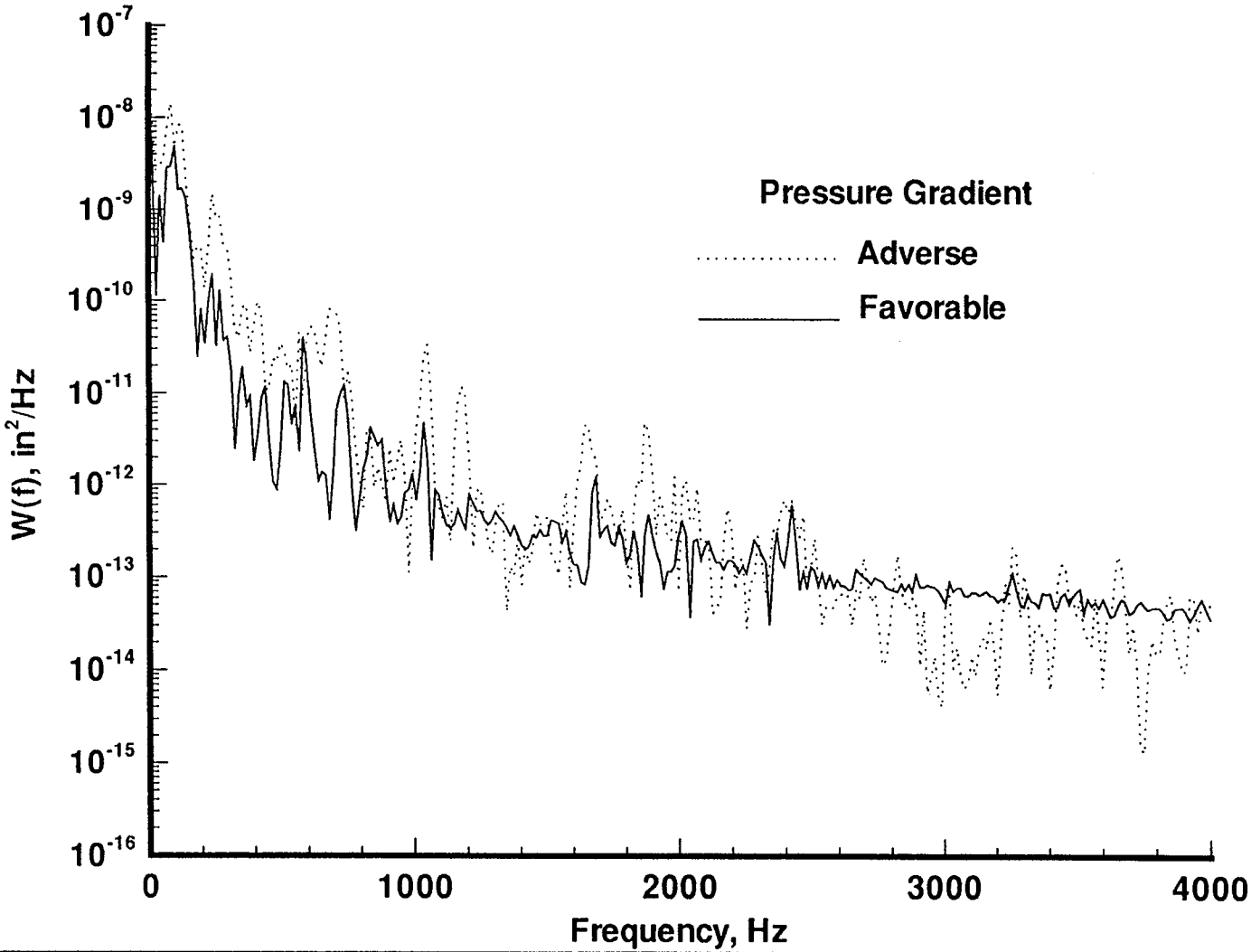

Figure 8: Time history of the radiated acoustic pressure 0.5 ft away from the center of the flexible plates. (a) From the adverse pressure gradient plate, (b) from the favorable pressure gradient plate and (c) from both plates.

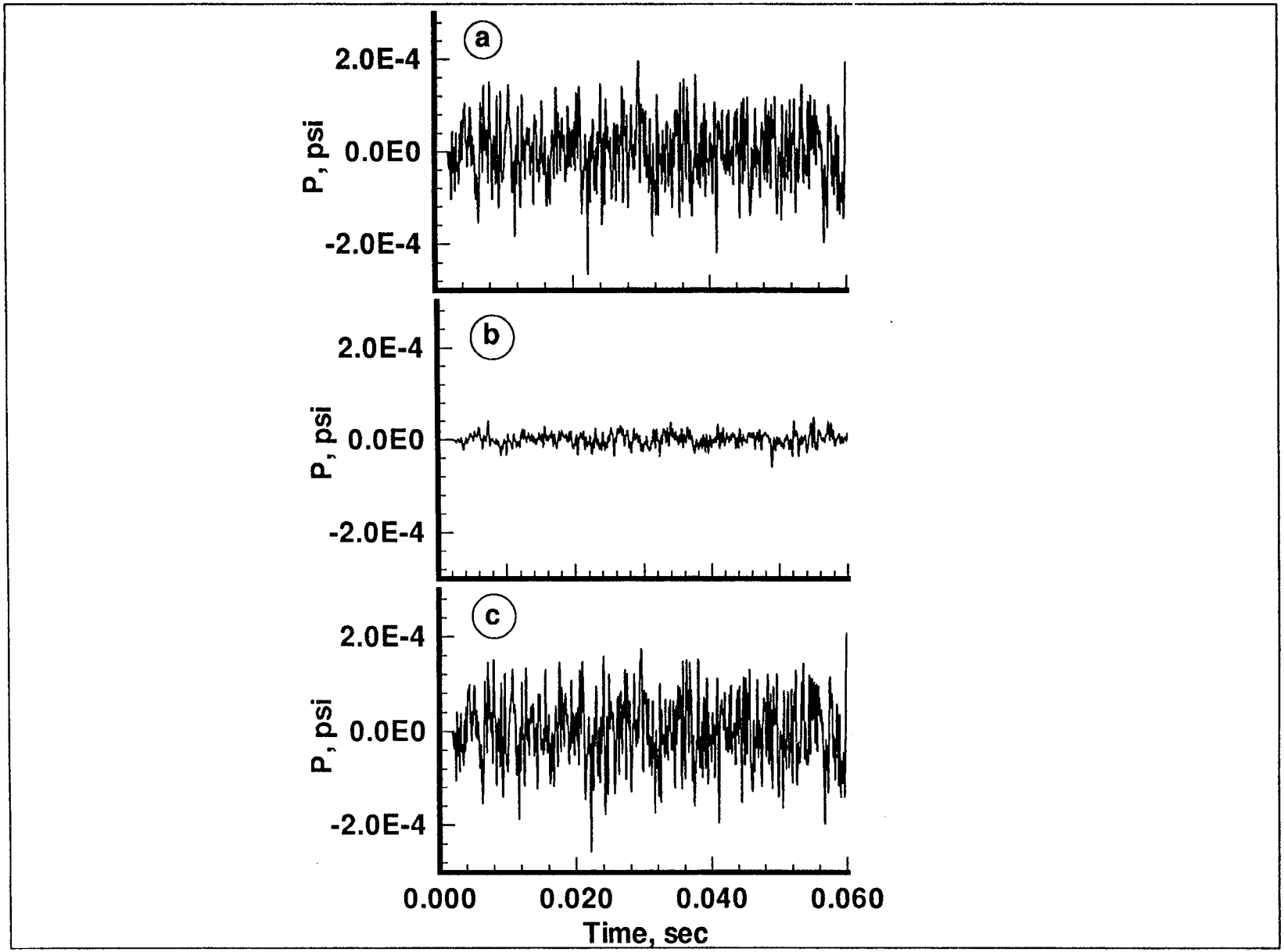

Figure 9: PSD of the radiated acoustic pressure 0.5 ft away from the center of the two flexible plates.

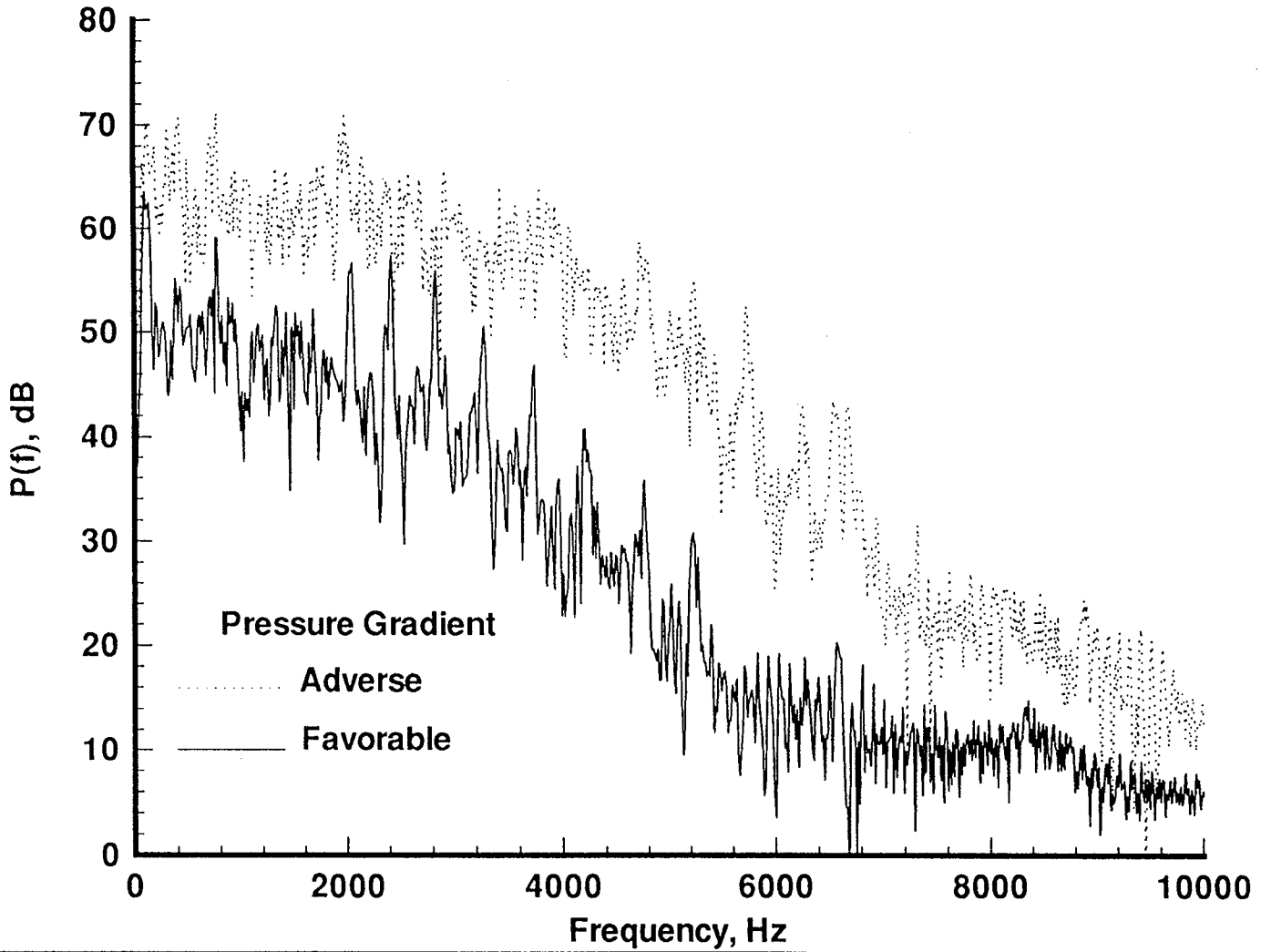

Figure 10: Fluid vertical velocity distribution over the rigid and flexible surfaces.

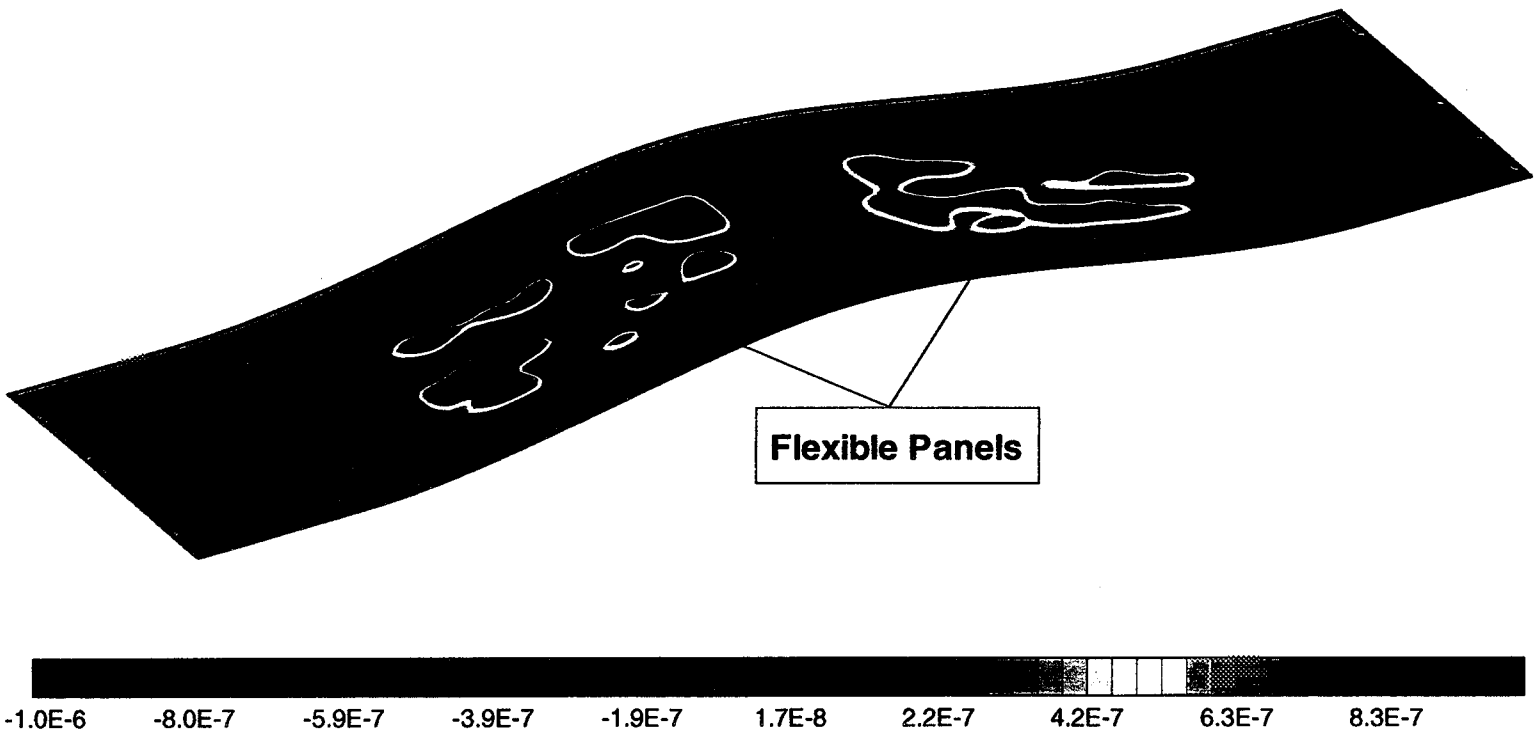

Figure 11: Instantaneous displacement response of the flexible plates.

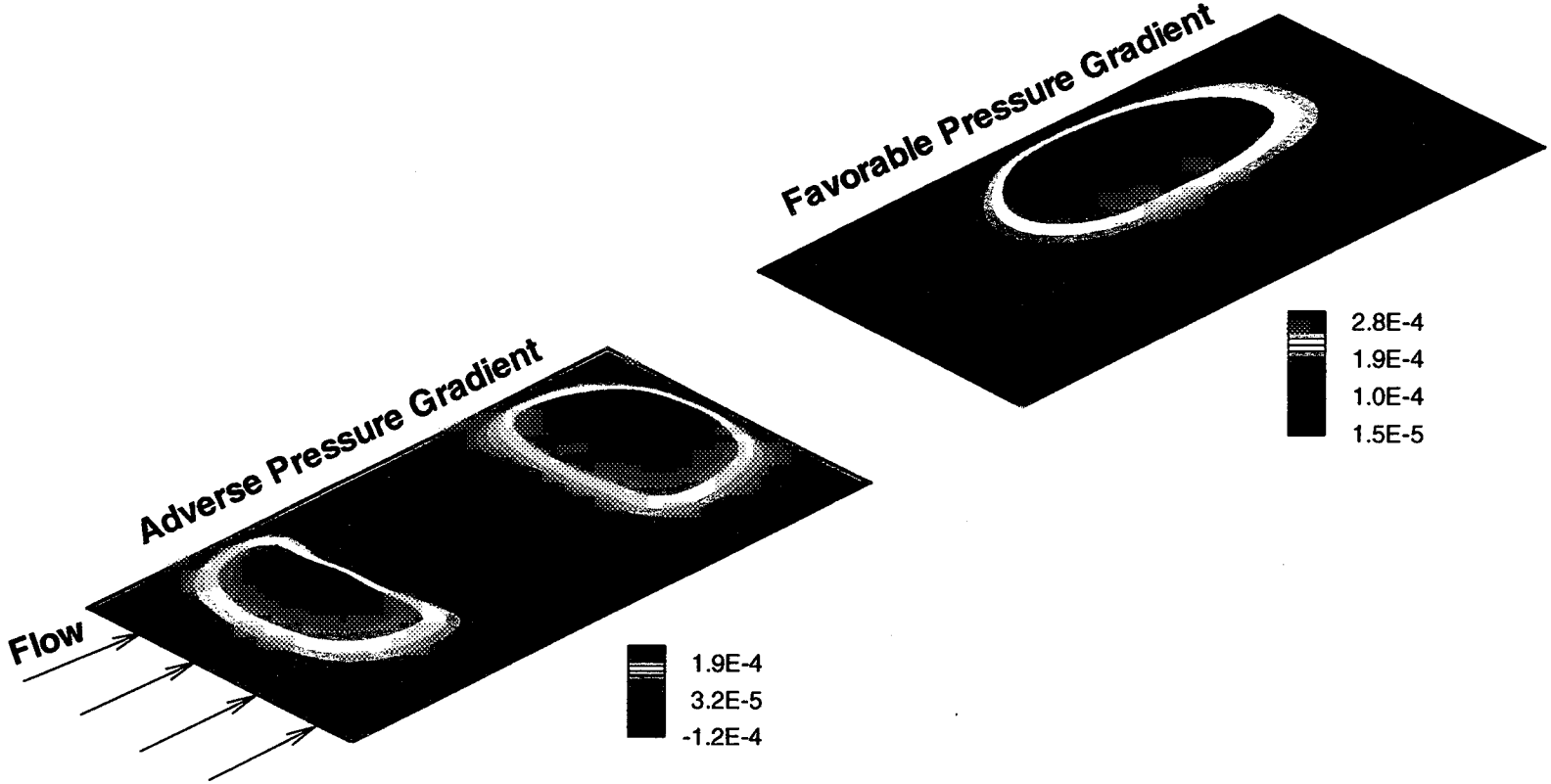

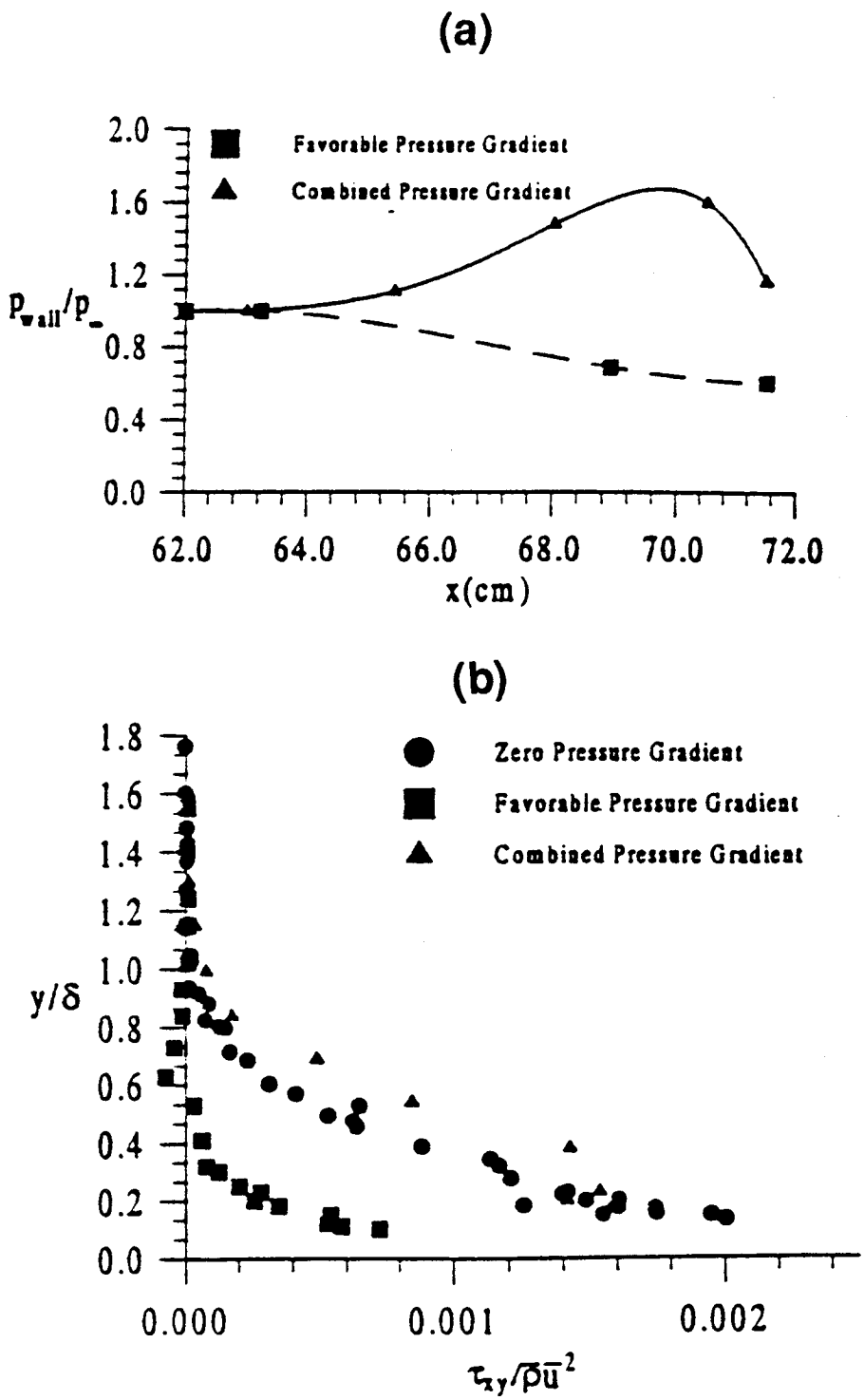

Figure 12: From Bowersox and Buter's paper [4], (a) Static pressure distribution along the streamwise direction, (b) Favre averaged Reynolds stresses.

Figure 13a: Static pressure distribution along the streamwise direction.

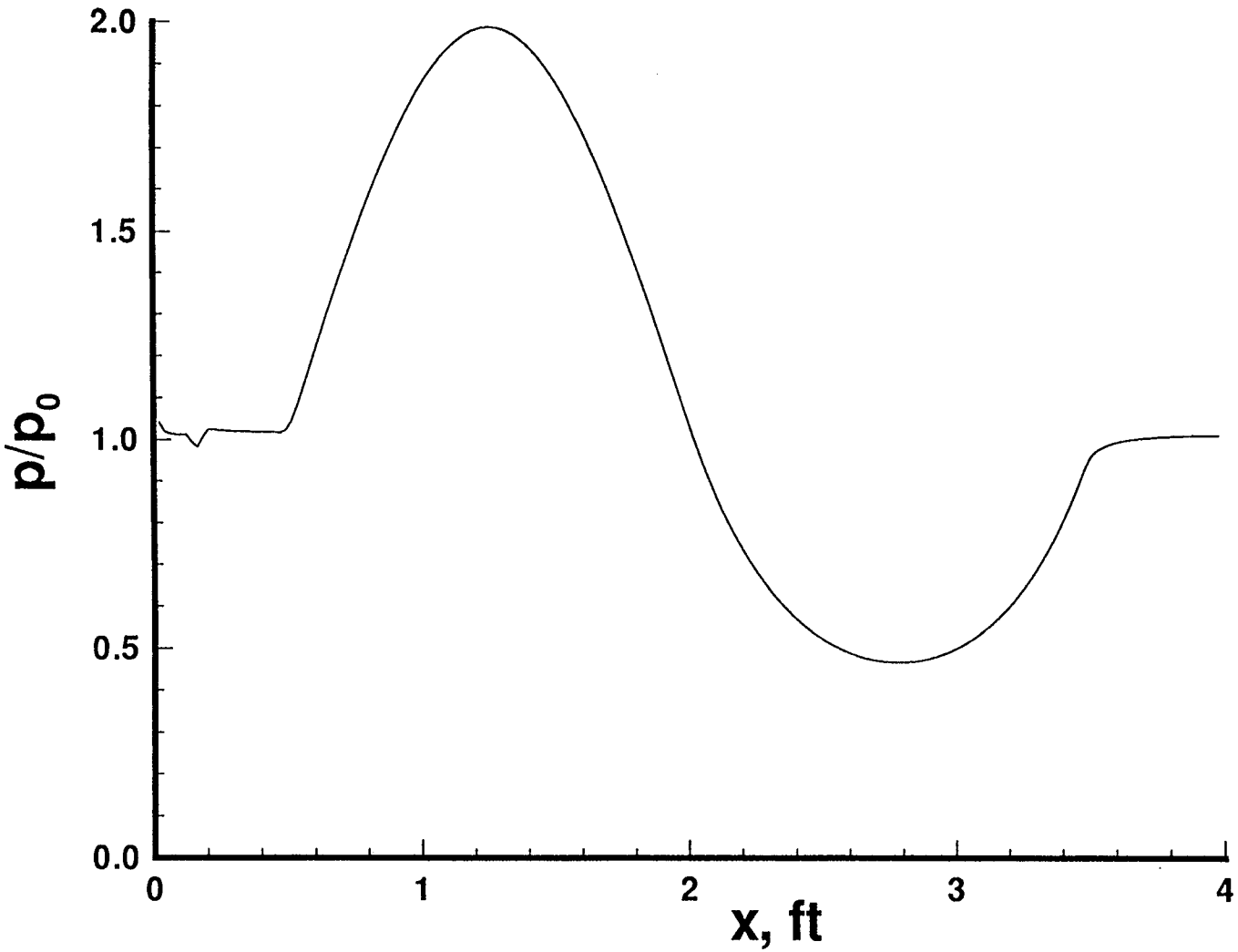

Figure 13b: Favre averaged Reynolds stresses as a function of the vertical distance.

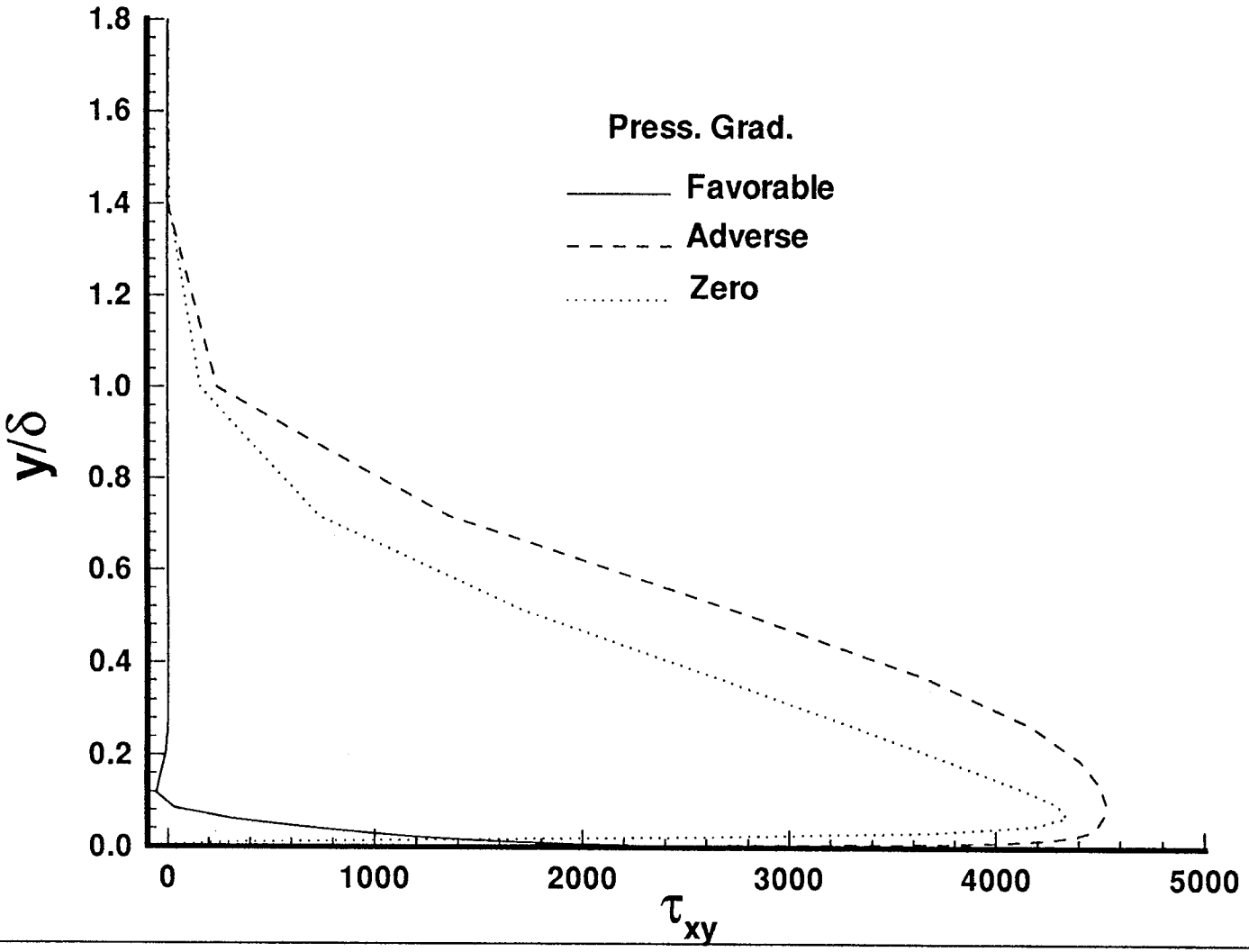

Figure 14: Mean velocity profile

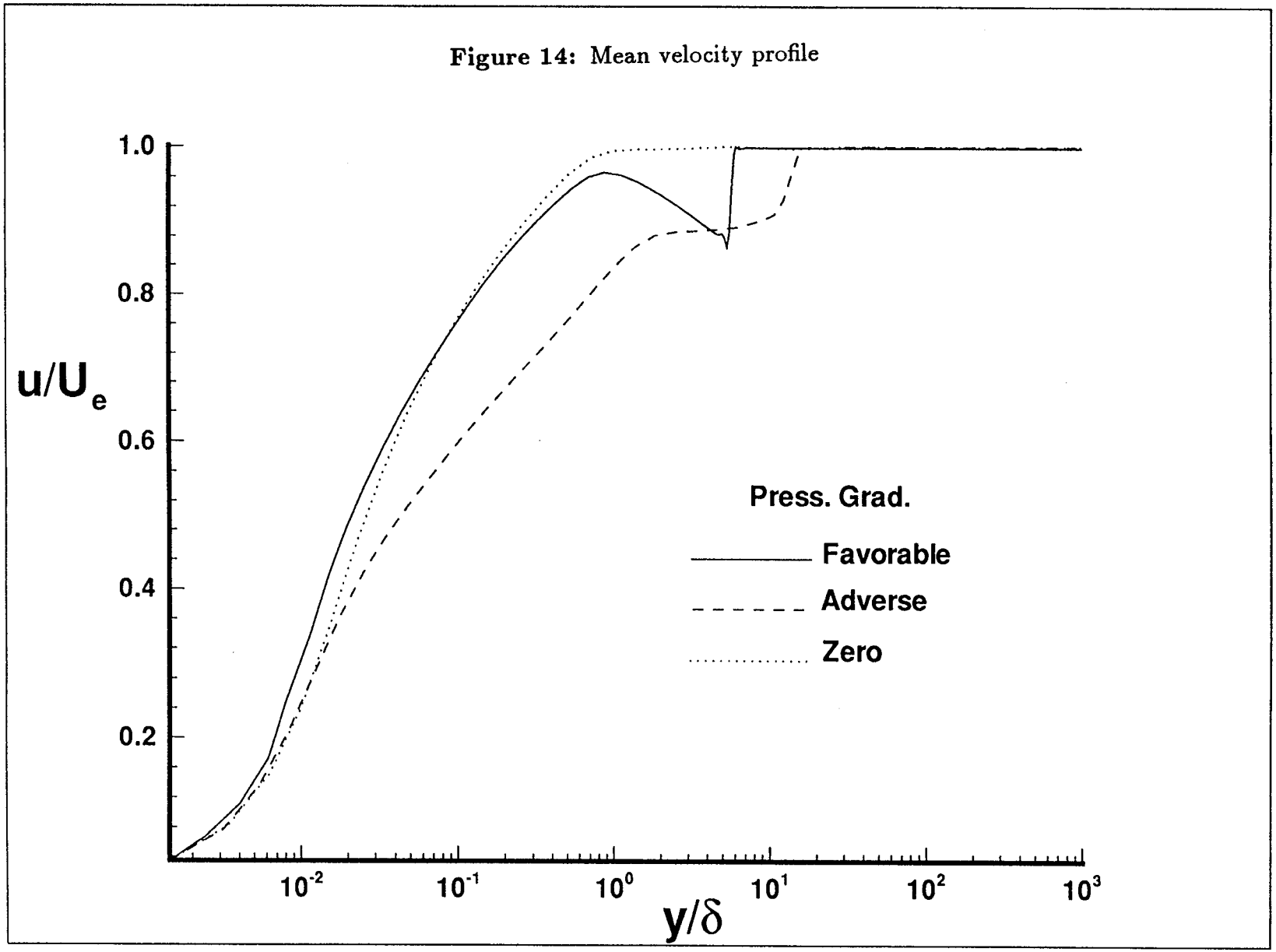

Figure 15: Friction coefficient as a function of the downstream distance.

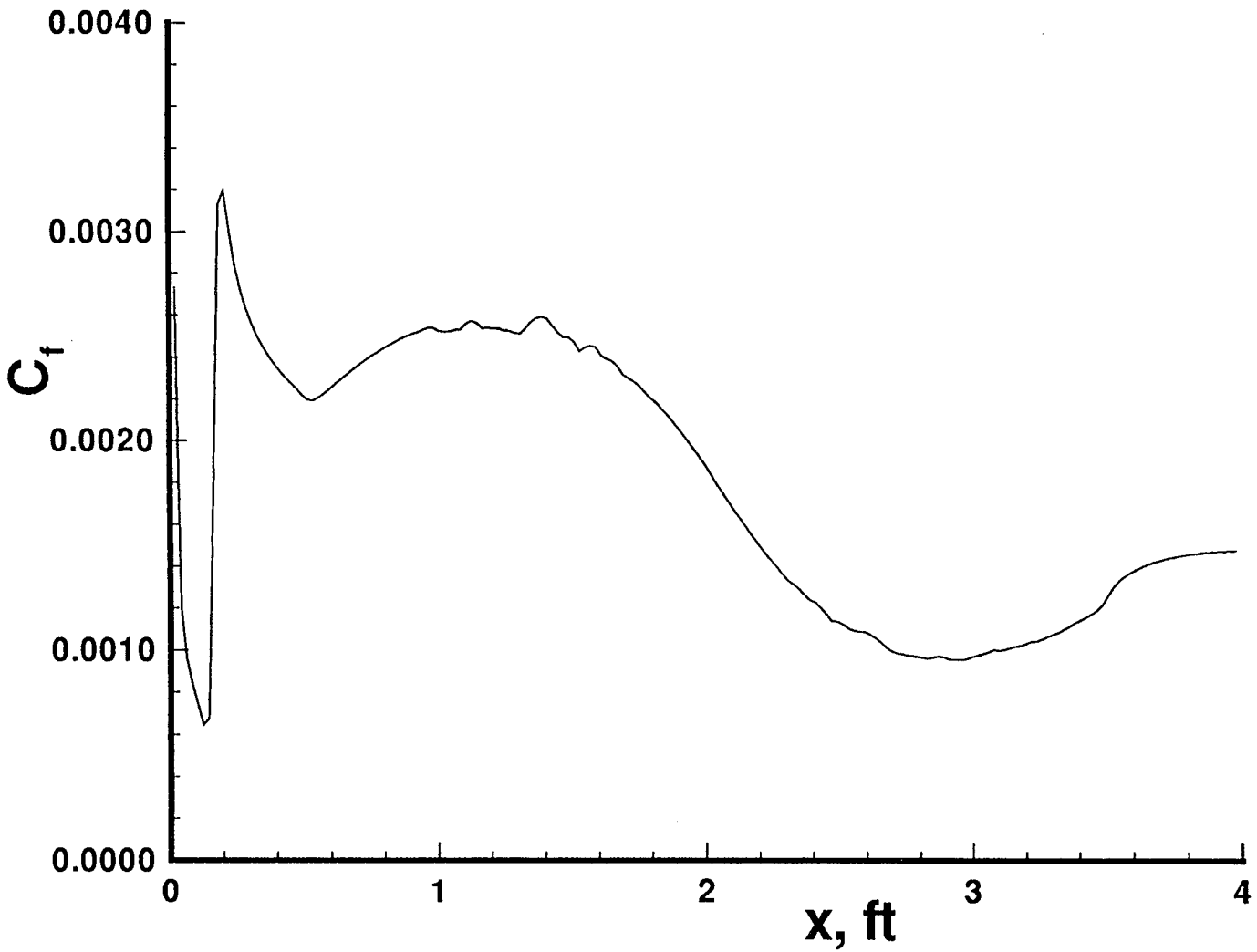

Figure 16a: Computational domain used in the favorable pressure gradient calculation.

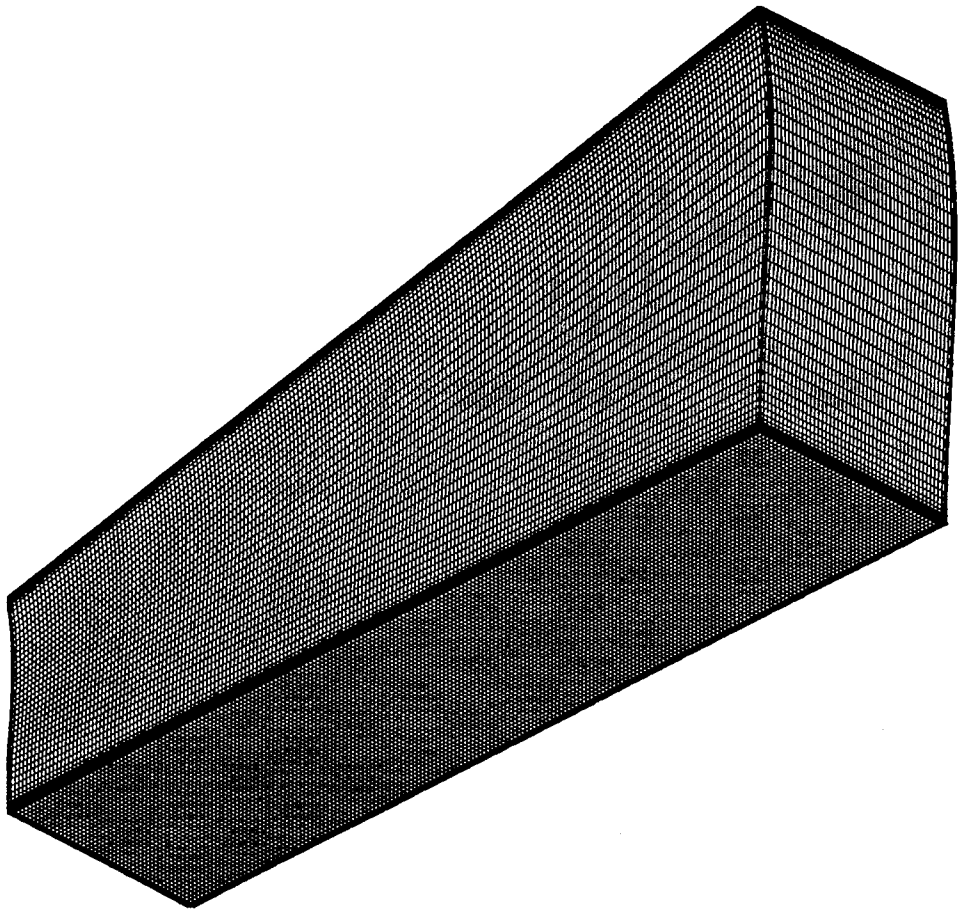

Figure 16b: Computational domain used in the adverse pressure gradient calculation.

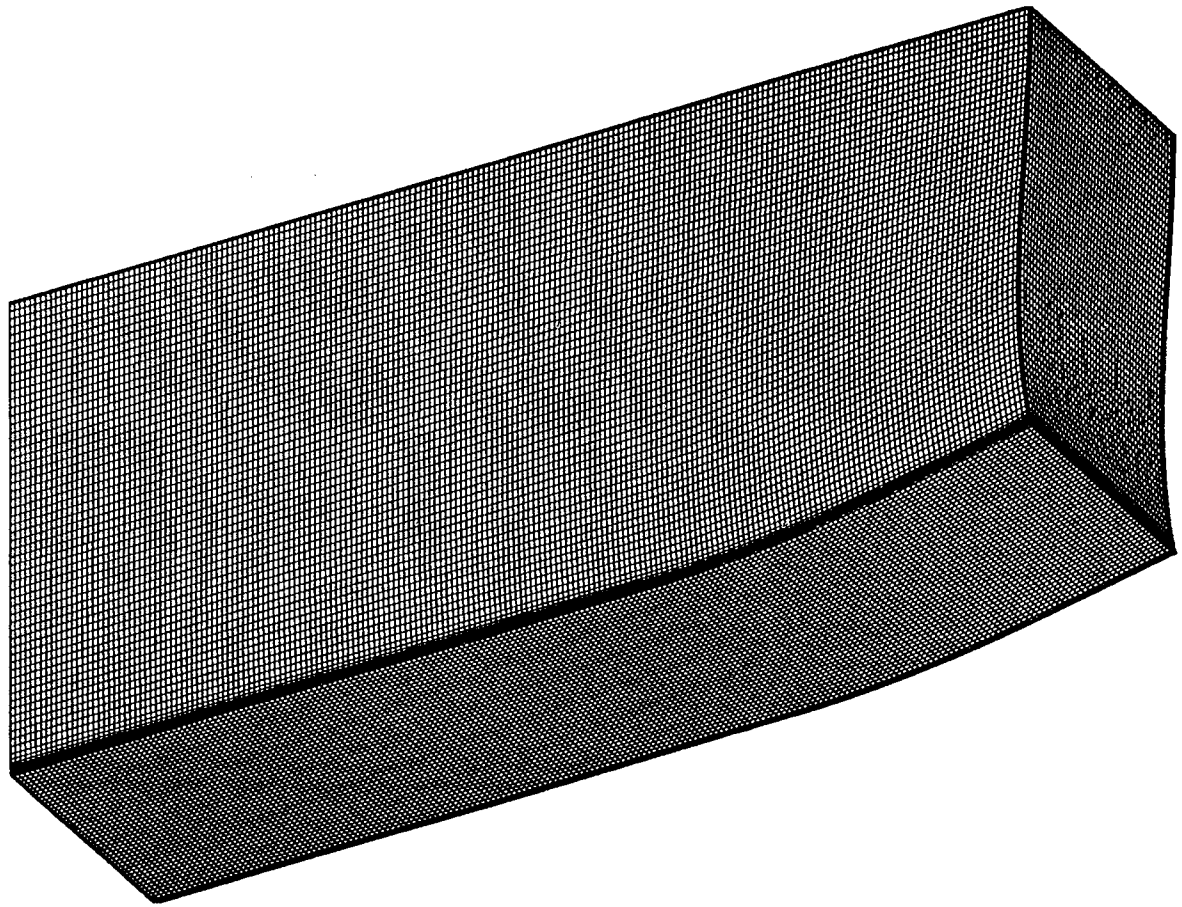

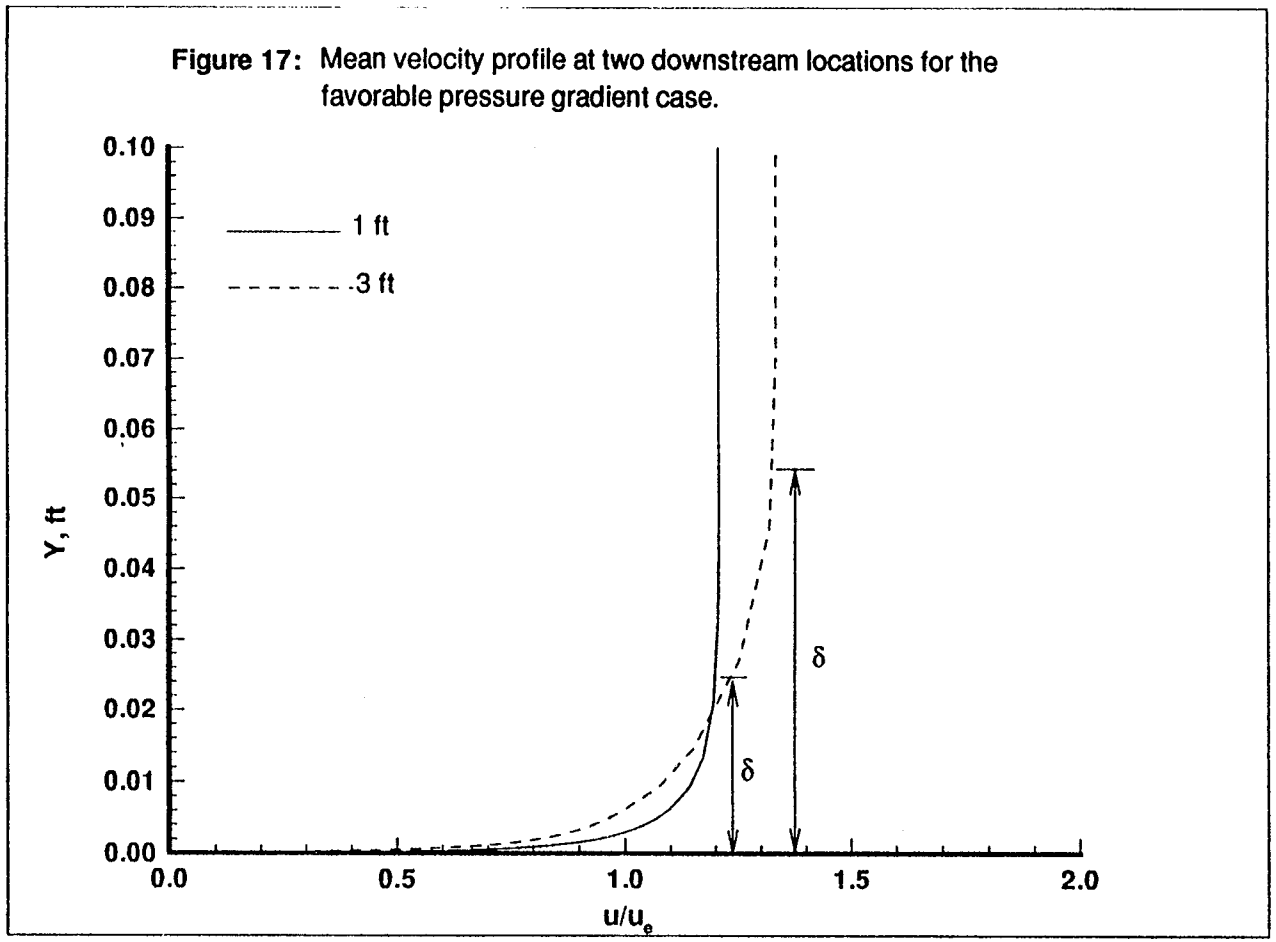

Figure 17: Mean velocity profile at two downstream locations for the favorable pressure gradient case.

Figure 18: Favorable pressure gradient: (a) PSD of the wall pressure fluctuation at the center of the flexible plate, (b) PSD of the displacement response at the center of the flexible plate.

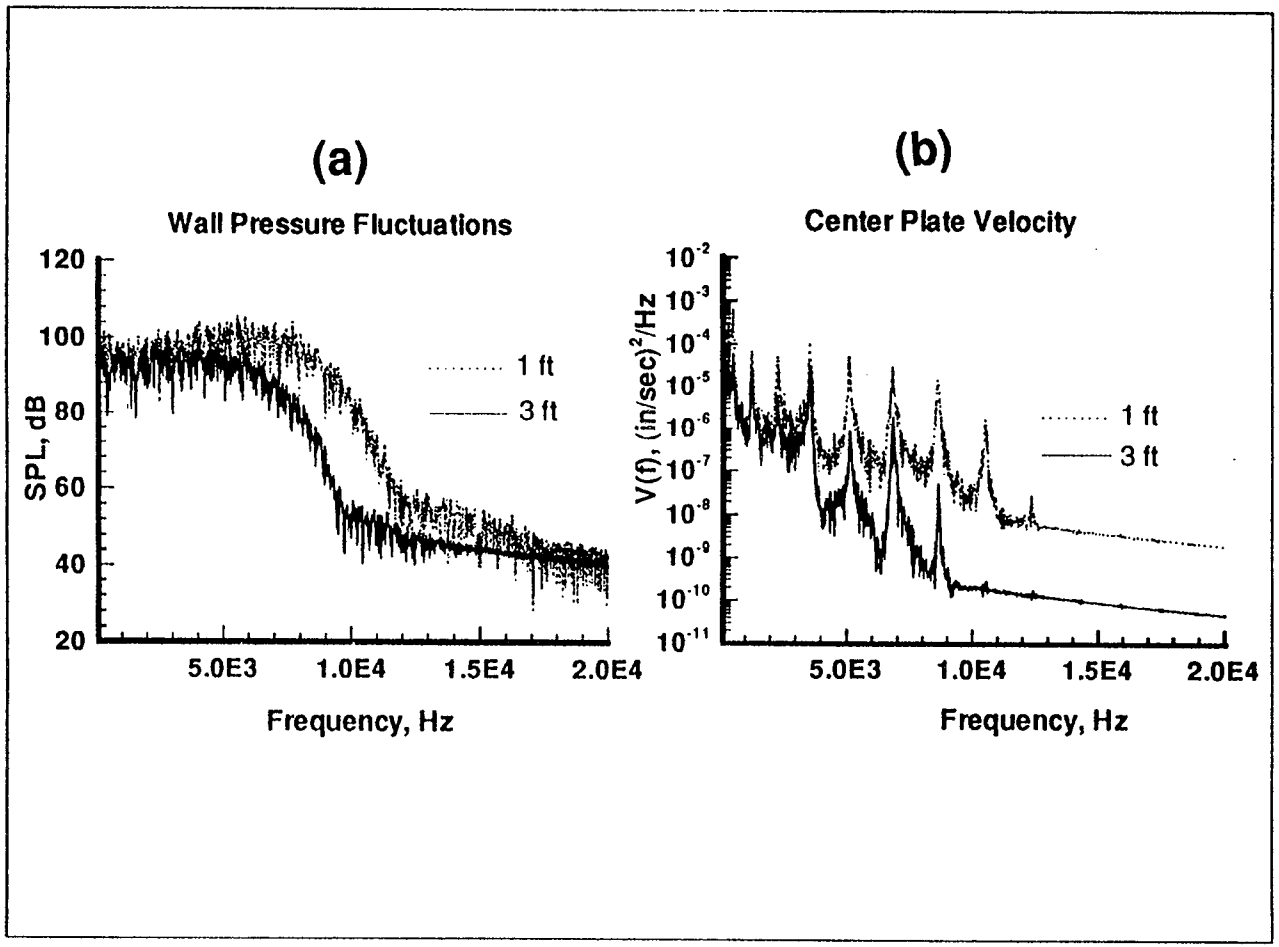

Figure 19: Adverse pressure gardient: (a)PSD of the wall pressure fluctuation at the center of the flexible plate, (b) PSD of the displacement response at the center of the flexible plate.

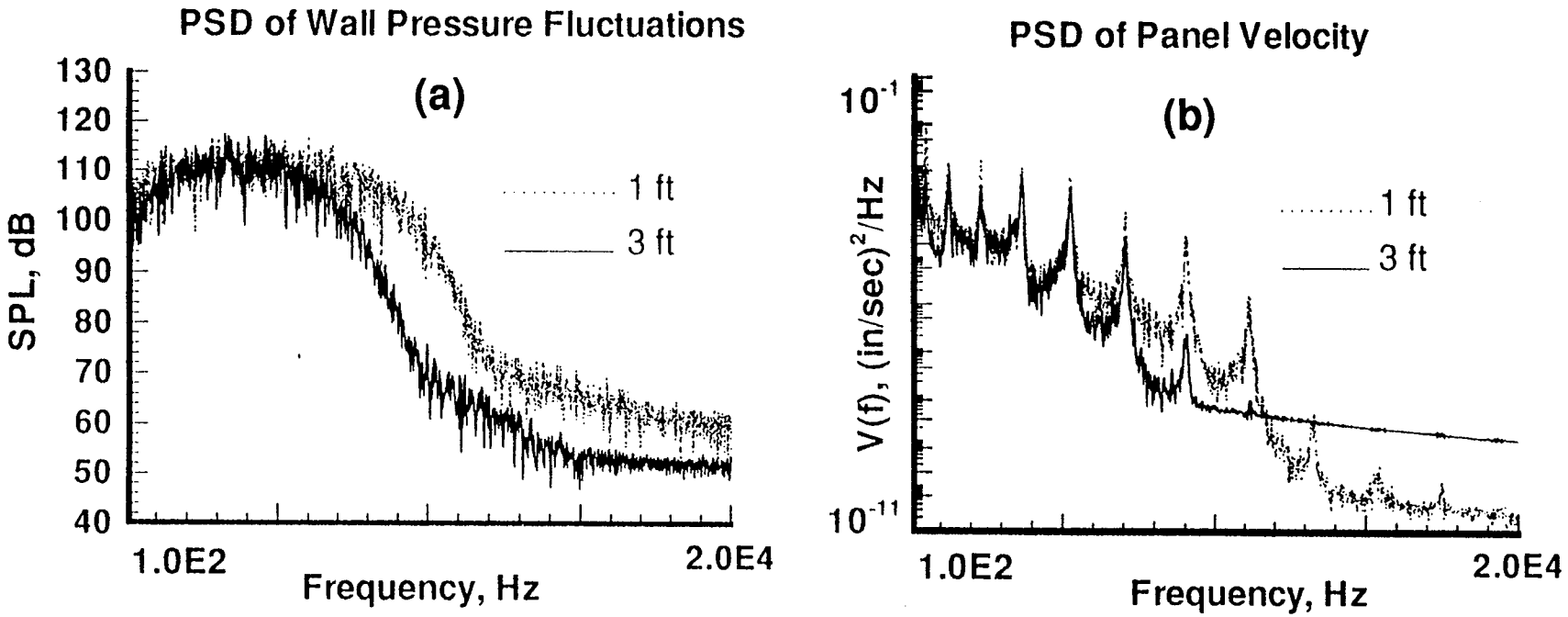

Figure 20: Favorable pressure gradient: (a) PSD of the wall pressure fluctuation at the center of the flexible plate, (b) PSD of the displacement response at the center of the flexible plate.

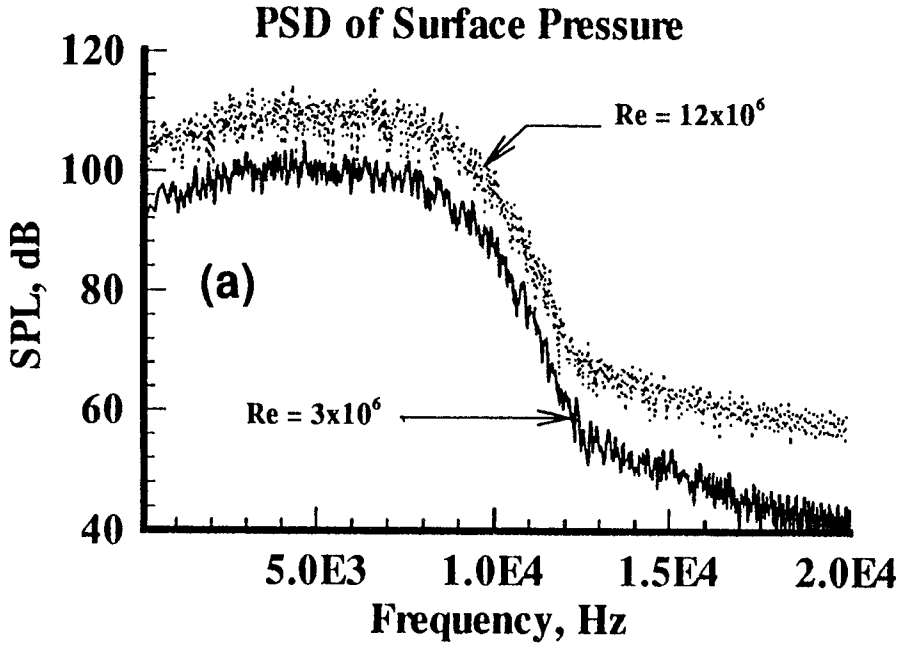

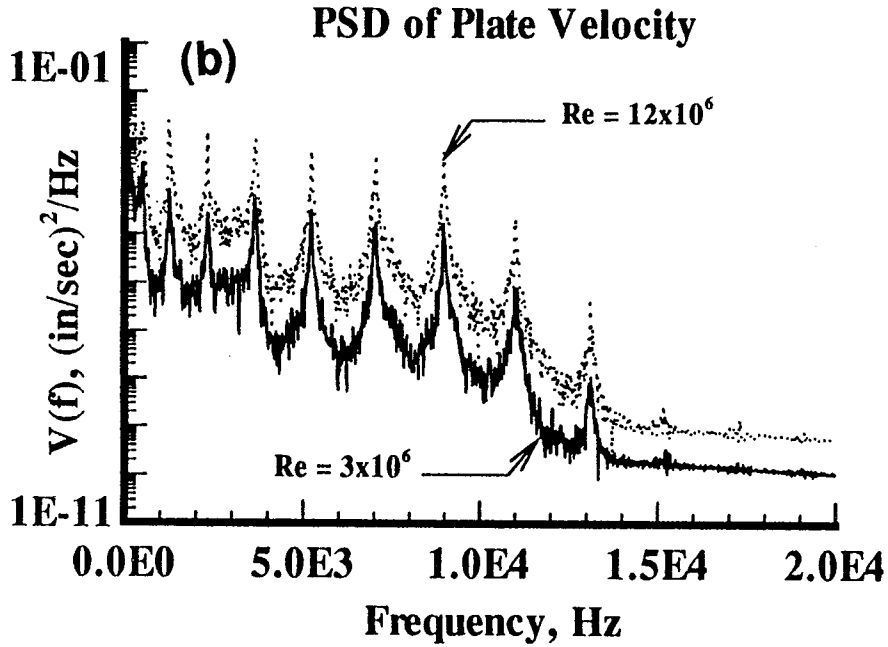

Figure 21: Adverse pressure gardient: (a)PSD of the wall pressure fluctuation at the center of the flexible plate, (b) PSD of the displacement response at the center of the flexible plate.

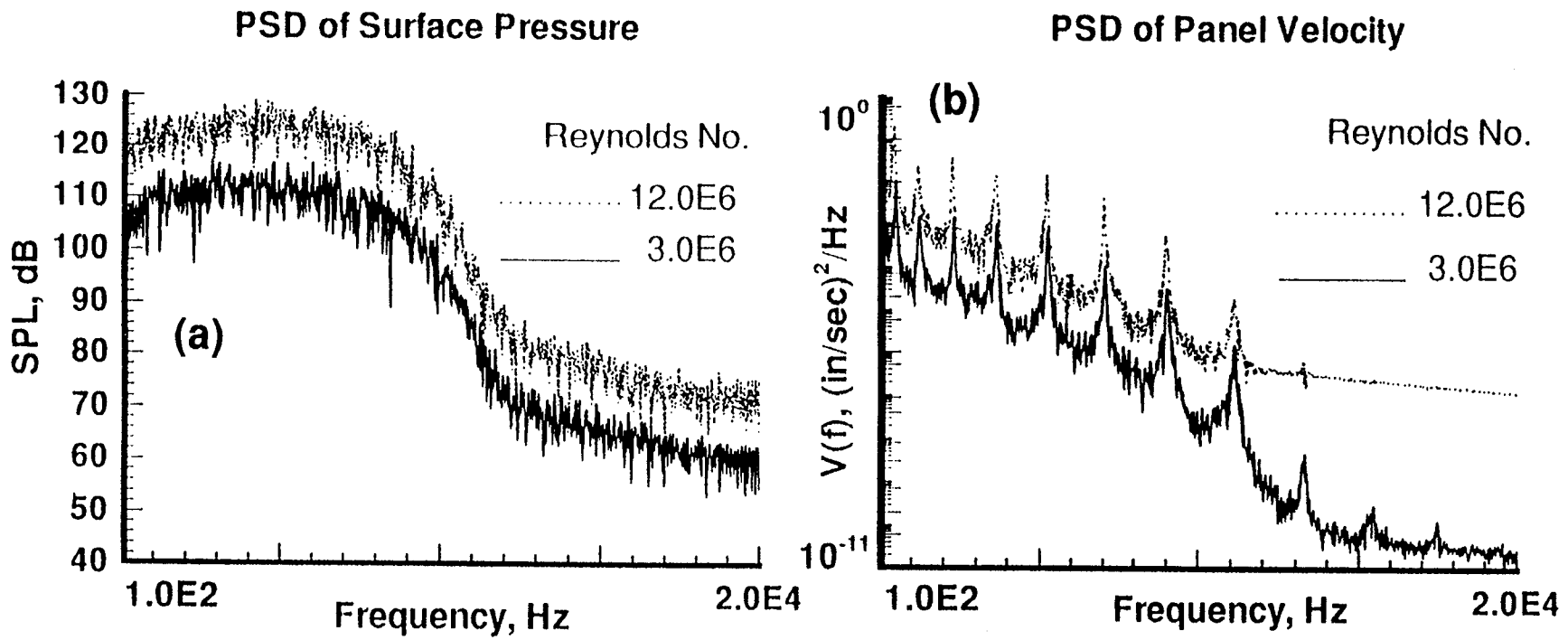

REPORT DOCUMENTATION PAGE

Form Approved
OMB No. 0704-0188

1. AGENCY USE ONLY *(Leave blank)*	2. REPORT DATE	3. REPORT TYPE AND DATES COVERED
	March 1997	Contractor Report

4. TITLE AND SUBTITLE
Effect of Pressure Gradients on Plate Response and Radiation in a Supersonic Turbulent Boundary Layer

5. FUNDING NUMBERS
C NAS1-19700/NAS1-96014
WU 537-06-37-20

6. AUTHOR(S)
Abdelkader Frendi

7. PERFORMING ORGANIZATION NAME(S) AND ADDRESS(ES)
Analytical Services and Materials, Inc.
Hampton, VA 23666

8. PERFORMING ORGANIZATION REPORT NUMBER

9. SPONSORING / MONITORING AGENCY NAME(S) AND ADDRESS(ES)
National Aeronautics and Space Administration
Langley Research Center
Hampton, VA 23681-0001

10. SPONSORING / MONITORING AGENCY REPORT NUMBER
NASA CR-201691

11. SUPPLEMENTARY NOTES
This work was supported under NASA Contracts NAS1-19700 to Analytical Services & Materials, Inc., and NAS1-96014, Lockheed Martin Engineering & Sciences, Hampton, VA, subcontract to Analytical Services & Materials, Inc. (Langley Technical Monitor: Stephen A. Rizzi)

12a. DISTRIBUTION / AVAILABILITY STATEMENT
Unclassified - Unlimited
Subject Category 71

12b. DISTRIBUTION CODE

13. ABSTRACT ***(Maximum 200 words)***

Using the model developed by the author for zero-pressure gradient turbulent boundary layers, results are obtained for adverse and favorable pressure gradients. It is shown that when a flexible plate is located in an adverse pressure gradient area, it vibrates more than if it were in a favorable pressure gradient one. Therefore, the noise generated by the plate in an adverse pressure gradient is much greater than that due to the plate in a favorable pressure gradient. The effects of Reynolds number and boundary layer thickness are also analysed and found to have the same effect in both adverse and favorable pressure gradient cases. Increasing the Reynolds number is found to increase the loading on the plate and therefore acoustic radiation. An increase in boundary layer thickness is found to decrease the level of the high frequencies and therefore the response and radiation at these frequencies. The results are in good qualitative agreement with experimental measurements.

14. SUBJECT TERMS
High-Speed Research; Adverse Pressure Gradient; Favorable Pressure Gradient; Pressure Gradients; Flexible Structure; Supersonic; Turbulent Boundary Layer; Dynamic Structural Response; Acoustic Radiation

15. NUMBER OF PAGES
36

16. PRICE CODE
A03

17. SECURITY CLASSIFICATION OF REPORT	18. SECURITY CLASSIFICATION OF THIS PAGE	19. SECURITY CLASSIFICATION OF ABSTRACT	20. LIMITATION OF ABSTRACT
Unclassified	Unclassified	Unclassified	